JOURNAL OF GEOPHYSICAL RESEARCH, VOL. 105, NO. B9, PAGES 21,591–21,614, SEPTEMBER 10, 2000

Crustal structure of the southeast Greenland margin from joint refraction and reflection seismic tomography

J. Korenaga,[1,2] W. S. Holbrook,[3] G. M. Kent,[4] P. B. Kelemen,[2] R. S. Detrick[2],
H.-C. Larsen,[5] J. R. Hopper,[5] and T. Dahl-Jensen[5]

Abstract. We present results from a combined multichannel seismic reflection (MCS) and wide-angle onshore/offshore seismic experiment conducted in 1996 across the southeast Greenland continental margin. A new seismic tomographic method is developed to jointly invert refraction and reflection travel times for a two-dimensional velocity structure. We employ a hybrid ray-tracing scheme based on the graph method and the local ray-bending refinement to efficiently obtain an accurate forward solution, and we employ smoothing and optional damping constraints to regularize an iterative inversion. We invert 2318 *Pg* and 2078 *PmP* travel times to construct a compressional velocity model for the 350-km-long transect, and a long-wavelength structure with strong lateral heterogeneity is recovered, including (1) ~30-km-thick, undeformed continental crust with a velocity of 6.0 to 7.0 km/s near the landward end, (2) 30- to 15-km-thick igneous crust within a 150-km-wide continent-ocean transition zone, and (3) 15- to 9-km-thick oceanic crust toward the seaward end. The thickness of the igneous upper crust characterized by a high-velocity gradient also varies from 6 km within the transition zone to ~3 km seaward. The bottom half of the lower crust generally has a velocity higher than 7.0 km/s, reaching a maximum of 7.2 to 7.5 km/s at the Moho. A nonlinear Monte Carlo uncertainty analysis is performed to estimate the a posteriori model variance, showing that most velocity and depth nodes are well determined with one standard deviation of 0.05-0.10 km/s and 0.25-1.5 km, respectively. Despite significant variation in crustal thickness, the mean velocity of the igneous crust, which serves as a proxy for the bulk crustal composition, is surprisingly constant (~7.0 km/s) along the transect. On the basis of a mantle melting model incorporating the effect of active mantle upwelling, this velocity-thickness relationship is used to constrain the mantle melting process during the breakup of Greenland and Europe. Our result is consistent with a nearly constant mantle potential temperature of 1270-1340°C throughout the rifting but with a rapid transition in the style of mantle upwelling, from vigorous active upwelling during the initial rifting phase to passive upwelling in the later phase.

1. Introduction

Igneous crust emplaced at a rifted continental margin is the integrated product of the melting of an upwelling mantle during continental breakup. Its thickness is often taken as a good proxy for the total melt volume produced upon rifting, whereas its seismic velocity reflects the original melt composition [e.g., *White and McKenzie*, 1989; *Kelemen and Holbrook*, 1995]. Because the mantle melting process is highly sensitive to the temperature and composition of the mantle as well as its upwelling rate [e.g., *McKenzie and Bickle*, 1988; *Kinzler and Grove*, 1992; *Langmuir et al.*, 1992], the crustal seismic structure of a rifted margin is one of the primary sources of information regarding mantle dynamics in the rifting period.

Rifted continental margins are often associated with voluminous igneous activity as inferred from seaward dipping reflectors (SDRs), which were proposed to originate in subaerial eruptions [*Hinz*, 1981; *Mutter et al.*, 1982], as later confirmed by deep-sea drilling [*Roberts et al.*, 1984; *Eldholm et al.*, 1989; *Larsen et al.*, 1994]. Deep seismic studies have revealed thick sequences of mafic igneous crust below SDRs on several margins [e.g., *White et al.*, 1987; *Mutter et al.*, 1988; *Holbrook and Kelemen*, 1993]; the thickness of such igneous crust can be as much as several times that of normal oceanic crust, indicating some unusual condition in mantle melting, such as higher-than-normal potential temperature and/or rapid mantle upwelling. The southeast Greenland margin, which was formed during the opening of the North Atlantic around 60 Ma [*Srivastava and Tapscott*, 1986], is one of these volcanic rifted margins; SDRs have been mapped over 2000 km along the entire margin [*Larsen and Jakobsdóttir*, 1988], and the crustal structure of the conjugate margin [*White et al.*, 1987; *Mutter and Zehnder*, 1988; *Barton and White*, 1997a] suggests the existence of similarly thick igneous crust beneath the SDRs. Because of its proximity to the Iceland hotspot, it has been proposed that a mantle plume played a major role in the formation of this volcanic margin [e.g., *Richards et al.*, 1989; *White and McKenzie*, 1989; *Hill et al.*, 1992; *Coffin and Eldholm*, 1994; *Barton and White*, 1997a], but the paucity of high-quality seismic data in this region has prevented a full understanding of the influence of a mantle plume on continental rifting magmatism.

[1]Department of Earth, Atmospheric, and Planetary Sciences, Massachusetts Institute of Technology, Cambridge.
[2]Department of Geology and Geophysics, Woods Hole Oceanographic Institution, Woods Hole, Massachusetts.
[3]Department of Geology and Geophysics, University of Wyoming, Laramie, Wyoming.
[4]Institute of Geophysics and Planetary Physics, Scripps Institution of Oceanography, San Diego, California.
[5]Danish Lithosphere Centre, Copenhagen, Denmark.

Copyright 2000 by American Geophysical Union.

Paper number 2000JB900188.
0148-0227/00/2000JB900188$09.00

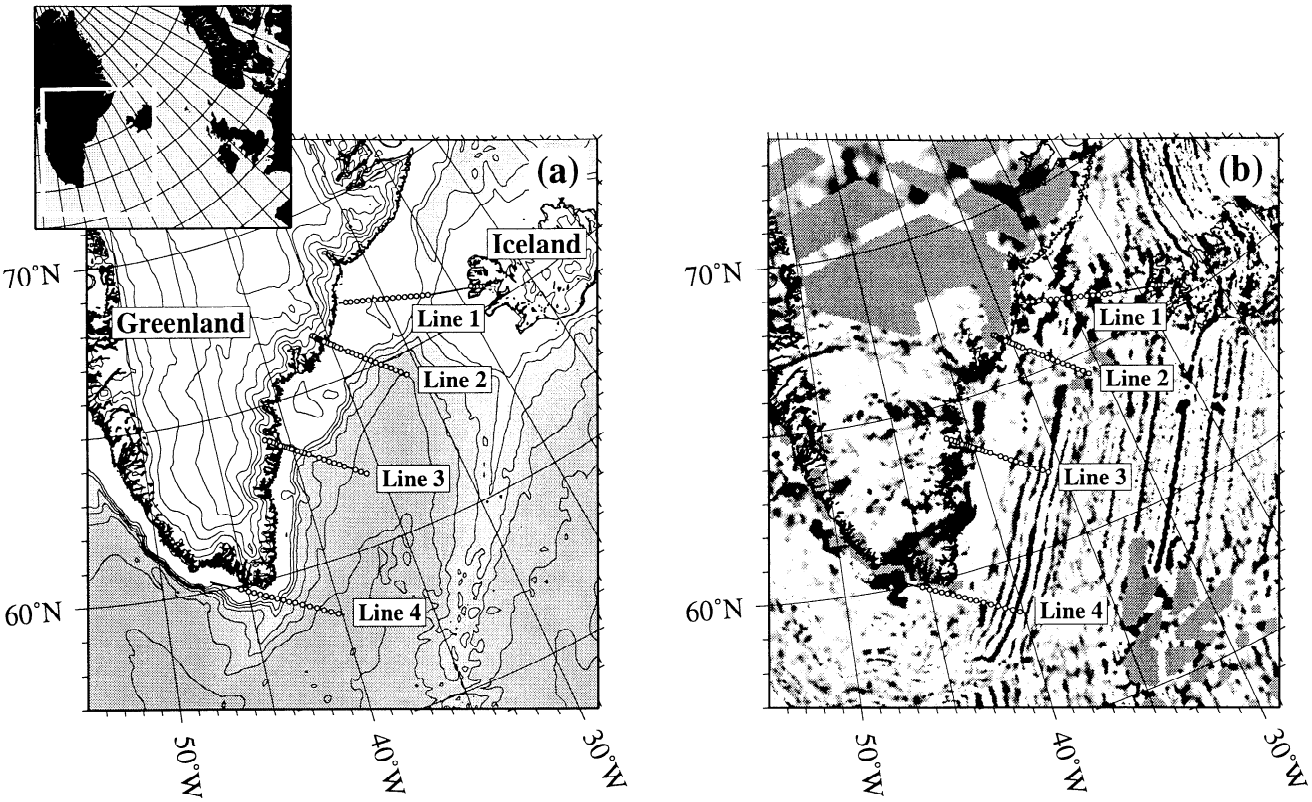

Figure 1. Location of the 1996 SIGMA seismic experiment. Circles denote location of onshore and offshore seismic instruments. (a) Bathymetry with 500-m contour interval. (b) Magnetic anomaly with positive anomaly shaded.

To investigate the influence of the Iceland hotspot on the opening of the North Atlantic, an extensive deep seismic experiment, the 1996 Seismic Investigation of the Greenland Margin (SIGMA), was conducted along the southeast Greenland margin jointly by Woods Hole Oceanographic Institution (WHOI) and the Danish Lithosphere Centre. Four transects were located at latitudes of approximately 68°N, 66°N, 63°N, and 59°N to systematically sample the structure of the margin at increasing distance from the Greenland-Iceland Ridge, the presumed Iceland hotspot track (Figure 1). This paper focuses on results from transect 2, whose data comprise ~300 km of multichannel seismic reflection data and coincident wide-angle refraction and reflection data recorded on 17 ocean bottom and eight onshore seismometers, covering from the Greenland coast through the continental shelf to the deep-water ocean basin at magnetic anomaly chron 19. Unlike the two transects to the south, linear marine magnetic anomalies are not observed on the northwestern part of transect 2 (Figure 1b), suggesting a significant deviation from normal seafloor spreading. Owing to its proximity to the hotspot track, the extent of rifting-to-spreading magmatism on this transect is critical to assess the possible effects of a mantle plume.

In this paper, we develop a joint refraction and reflection tomographic method to invert wide-angle travel time data for a compressional velocity field. The forward travel time calculation takes a hybrid approach; a graph-theoretical method is used to ensure a global optimization, followed by ray-bending refinement to achieve the desired accuracy. The inversion with a fine model parameterization is regularized by smoothness constraints on both velocity and reflector nodes. Velocity-depth ambiguity is always a serious concern for reflection tomography, and we show a simple and practical way to investigate the ambiguity using depth kernel weighting. The uncertainty of a velocity model is also estimated by a nonlinear Monte Carlo approach. The crustal structure of the volcanic continental margin, which exhibits strong lateral heterogeneity both in velocity and crustal thickness, is shown to be fully resolved with high model fidelity, and we discuss its geological and geophysical implications.

2. Data Acquisition and Processing

The seismic data on transect 2 of the SIGMA experiment were acquired in September 1996 aboard R/V *Maurice Ewing*. Multichannel seismic (MCS) profiling was conducted using a 20-element, 8460 cubic inch air gun array fired every ~50 m (20 s) and a 4.0-km hydrophone streamer with 160 channels. Wide-angle data were recorded on 10 WHOI ocean bottom hydrophones (OBH), eight U.S. Geological Survey (USGS) ocean bottom seismometers (OBS), and eight on-land seismic recorders from the Program for the Array Seismic Studies of the Continental Lithosphere (PASSCAL), deployed along the transect (Figure 2). We will hereafter refer to model distance along the transect, which is measured from a point located ~5 km northwest of the most landward seismometer, ST 9. The total model distance of transect 2 is 350 km.

2.1. Multichannel Seismic Data

Shot gathers were recorded at a sampling interval of 4 ms. Streamer group spacing was 25 m, which gives a common

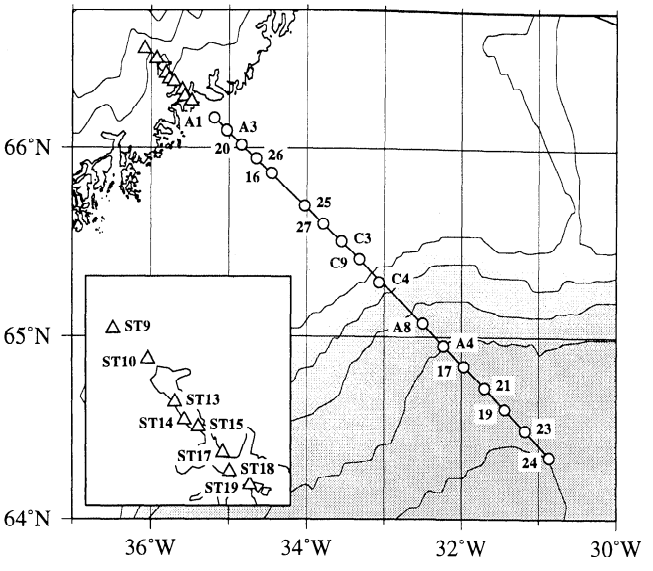

Figure 2. Configuration of transect 2 seismic experiment. Circles and triangles denote ocean bottom instruments and onshore seismic recorders, respectively. Bathymetry contours are drawn at 500-m interval.

midpoint (CMP) spacing of 12.5 m. With 160 channels and a shot interval of 50 m, CMP gathers sorted from raw shot gathers are thus 40-fold at maximum. After band-pass filtering from 5 to 40 Hz and a spherical divergence correction, stacking velocity analysis was conducted with four-CMP supergathers. In addition to strong seafloor and basement reflections, several sedimentary reflections were available to estimate stacking velocities. There are a few subbasement reflectors such as SDRs for some locations, but the majority of data do not exhibit coherent reflections below the basement. We thus used a velocity model based on wide-angle seismic data to supply stacking velocities for the crustal section. Because of severe sea conditions during the shooting of transect 2, the MCS data are only of modest quality, suffering from inconsistent gun signature, missing traces, and high ambient noise. Even with constant velocity stack analysis, no clear Moho reflection was identified throughout the transect. The following analysis therefore focuses only on the imaging of shallow crustal structure.

Our major task in MCS data processing was multiple suppression. Though it is not imperative for the deep-water environment, where the first water multiple occurs far below the basement, contamination by strong water multiples becomes more problematic as the seafloor shallows from km 250 landward on the transect. Unfortunately, the shallower bathymetry coincides with the occurrence of the SDR sequence, which is almost completely overlapped by high-energy water multiples. We first tried predictive deconvolution both in the t-x and τ-p domains with little success, probably because of low data quality. We found that the f-k demultiple method [e.g., *Yilmaz*, 1987] was more robust with negligible transform artifacts. To avoid aliasing, we applied the f-k multiple suppression to four-CMP supergathers with optional zero traces filling in missing offsets. We further applied a 2-km inside mute below the basement reflection because water multiples tend to be more coherent at smaller offsets in CMP gathers. Finally, a stacked time section was produced with median stacking, which turned out to be very effective in reducing any residual multiple energy; this is mainly because of a differential move-out between primary reflections and water multiples.

To correctly relocate reflectors in the depth section and collapse diffraction hyperbolae due to rough reflector topography, poststack depth migration was performed using the split-step migration algorithm [*Stoffa et al.*, 1990]. The velocity model based on the wide-angle data was used again for the crustal section in the migration. Except for several migration artifacts originating in missing data spots on the landward side, the overall quality of the migrated image is good, clearly depicting the sedimentary layers, the basement topography, and the intrabasement SDR sequence (Figure 3).

Sedimentary layers start to appear at km 113 and gradually thicken seaward, reaching a maximum thickness of ~1.5 km around the shelf break. The deep-water ocean basin is covered with <1-km-thick sediments. A distinct wedge of SDRs can be seen from km 190 to km 235; the reflectors are divergent arcuate with dips steepening from subhorizontal at shallow crustal levels to ~4° toward their base, and they can be traced to at least 4 km below the basement. The seaward end of the SDR sequence is abrupt, and it is marked by a basement high centered at km 240. The basement topography becomes more irregular seaward of the basement high, suggesting a transition from subaerial volcanism with extensive lava flows to more restricted submarine volcanism at this location. The continental side of the main SDR sequence may continue subhorizontally to km 120, though its reflectivity is more subdued. Apart from this, there is a strong dipping reflector running from km 80-150 (reflector A in Figure 3). Its reflectivity is unusually intense compared with other SDRs on this transect, generating its own strong water multiples. It is clear from its two-way travel times that the reflection is neither a seafloor multiple nor a basement multiple, so it must represent some sort of unconformity. The strong reflectivity, together with the lack of concurrent reflectors, suggests that it may represent a tectonic breakup unconformity as suggested by *Larsen and Duncan* [1996] for a similar reflector in the nearby EG66 seismic transect. However, as we will demonstrate with a tomographic image later, the reflector lies in the middle of the thick volcanic layer characterized by a high-velocity gradient, so that its origin remains uncertain.

2.2. Wide-Angle Seismic Data

Most of the wide-angle data on transect 2 are of high quality (Figure 4). The sampling interval was 10 ms, and 5-14 Hz band-pass filtering was applied to the data followed by predictive deconvolution and coherency weighting. Air gun firing at a 20-s interval at 4.7 knots yields densely spaced seismic traces at 50 m, and the resultant high phase correlation among traces is essential for accurate phase identification, especially for later arrivals such as *PmP*. One drawback of the short shooting interval, however, is that the reverberation of seismic energy in the water column can appear as strong "previous shot noise" [*Nakamura et al.*, 1987]. Though the air gun firing adapted a shot time randomization of ±1 s to reduce intertrace coherency of the waterborne energy, the sheer intensity of previous shot noise can be a major annoyance in a deep-water environment where water multiples can propagate to large offsets with little attenuation. To mitigate this problem, additional shooting with a 70-s interval was conducted for the wide-angle data acquisition on this transect. Without substantially sacrificing phase correlation the effect of previous shot noise is significantly reduced in the 70-s shot data, which were especially useful for phase interpretations with deep-water instruments.

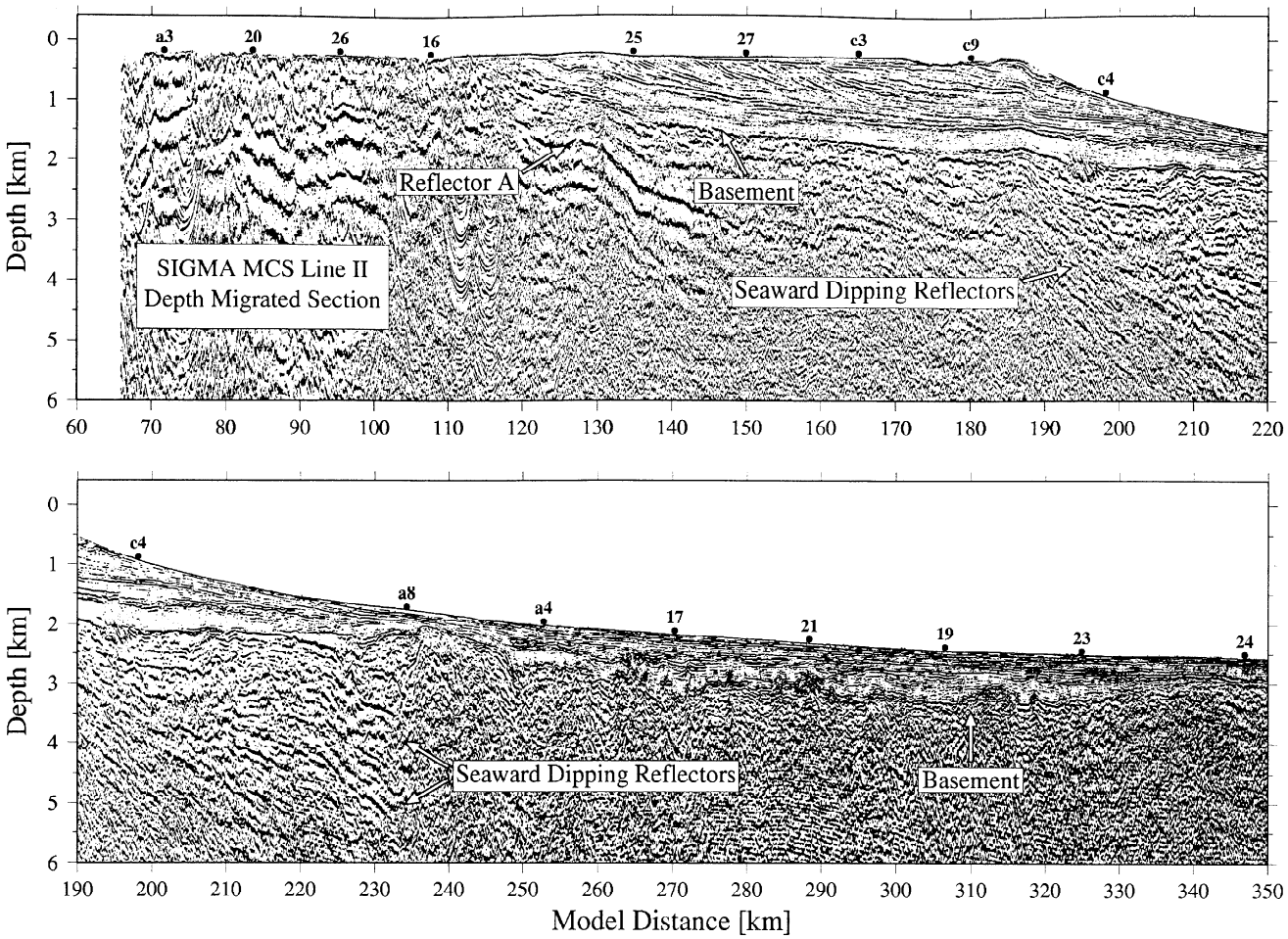

Figure 3. Depth-migrated section of multichannel seismic reflection profile. Coherence filtering, automatic gain correction, and trace normalization were applied. Locations of ocean bottom instruments are also shown by solid circles.

The refraction phase through the crystalline crust, *Pg*, is observed on all the instruments. The pattern of the *Pg* arrival varies significantly from deep-water instruments to shallow-water and on-land instruments, indicating a strong lateral variation in the crustal structure along the transect. The maximum range of the *Pg* arrivals increases from ~70 km in deep water to ~150 km along the inner continental shelf, indicating landward thickening of the high-velocity gradient upper crust. The near-offset asymmetry observed in *Pg* arrivals on OBH 20 (Figure 4g) suggests a sharp transition in the shallow upper crustal velocity at km ~80 because of the nearly flat basement and absence of sediment cover around the instrument. The apparent velocity of first arrivals rarely exceeds 7.0 km/s, so we do not have clear observation of refraction phase through the shallow upper mantle, *Pn*, in this seismic experiment. The absence of *Pn* phase is common in volcanic rifted margins [e.g., *Holbrook et al.*, 1994a, 1994b], and this may be because of high lowermost crustal velocities with possible cumulates increasing downward, which causes a broad transition in *P* wave velocity into the mantle.

The reflection phase from the crust-mantle boundary, *PmP*, is observed on most of the instruments with variable quality. The smallest offset where *PmP* arrivals can be recognized ranges from ~20 km in the deep ocean basin to 60-80 km on the continental shelf, and most of the *PmP* arrivals can be traced to merge with the *Pg* arrivals. Several minor midcrustal reflections are also observed on some instruments, but we do not attempt to model them because the number of such observations appears too small to confidently resolve causative geological structure. Being a later arrival, the *PmP* phase tends to be obscured by source-generated noise, and it is also sometimes difficult to distinguish it from midcrustal reflections and their multiples. The self-consistent identification of the *PmP* phase was made possible by confirming reciprocity among a number of different source-receiver pairs. For the on-land stations, however, reciprocity cannot be confirmed owing to the lack of land sources, and we relied on the phase correlation among the closely located stations. Refraction and reflection travel times were picked manually, and we assigned a picking error of half a period of the first cycle of an arrival, varied from 50 to 100 ms, to each picked travel time. Note that this criterion of assigning a picking error resulted in generally smaller data uncertainty than that used by W. S. Holbrook et al. (Mantle thermal structure and melting processes during continental breakup in the North Atlantic, submitted to *Earth and Planetary Science Letters*, 2000, hereinafter referred to as Holbrook et al., submitted manuscript, 2000). The new picking errors are used in this study because we realized that the previous estimate was less consistent and often too conservative.

3. Joint Refraction and Reflection Tomography

3.1. Model Parameterization

A two-dimensional velocity model is parameterized as a sheared mesh hanging beneath the seafloor and land surface

[*Toomey et al.*, 1994; *Van Avendonk et al.*, 1998]. Bilinear interpolation is used in each parallelogram-shaped grid cell, so the velocity field is continuous everywhere. Nodal spacing can be variable both in the horizontal and the vertical directions, and it should be much finer than expected velocity variations to avoid any bias introduced by a coarse parameterization. A fine mesh is also important to obtain accurate graph theoretical solutions. The sheared mesh representation allows accurate travel time calculation in the presence of large topographic variations, with much smaller computational resources than a rectangular grid used in some previous tomographic studies [e.g., *White and Clowes*, 1990; *Zhang and Toksöz*, 1998].

A reflector is represented as an array of linear segments, whose nodal spacing is independent of that used in the velocity grid. The horizontal coordinate of reflector nodes is fixed so that each node has only one degree of freedom in the vertical direction. Currently, only one reflector is supported in our method, which we used to model the *PmP* phase. Although the velocity discontinuity at the Moho is fundamental for the generation of the *PmP* phase, we do not explicitly treat this discontinuity in our modeling. Instead, we chose to employ a floating reflector formulation so that a reflector depth is updated freely without changing adjacent velocity nodes.

3.2. Forward Problem

The accurate and efficient calculation of travel times and ray paths is essential in seismic tomography. With a sampling interval of 10 ms and an average spacing of a few hundred meters in a velocity grid, our target accuracy is 1 ms in travel times and 100 m in ray path positions. We employ a hybrid method based on the graph method and the ray-bending method, similar to the one developed by *Papazachos and Nolet* [1997] and *Van Avendonk et al.* [1998], because it is probably most efficient in terms of both memory and computation time. The graph method, also known as the shortest path method, was developed in

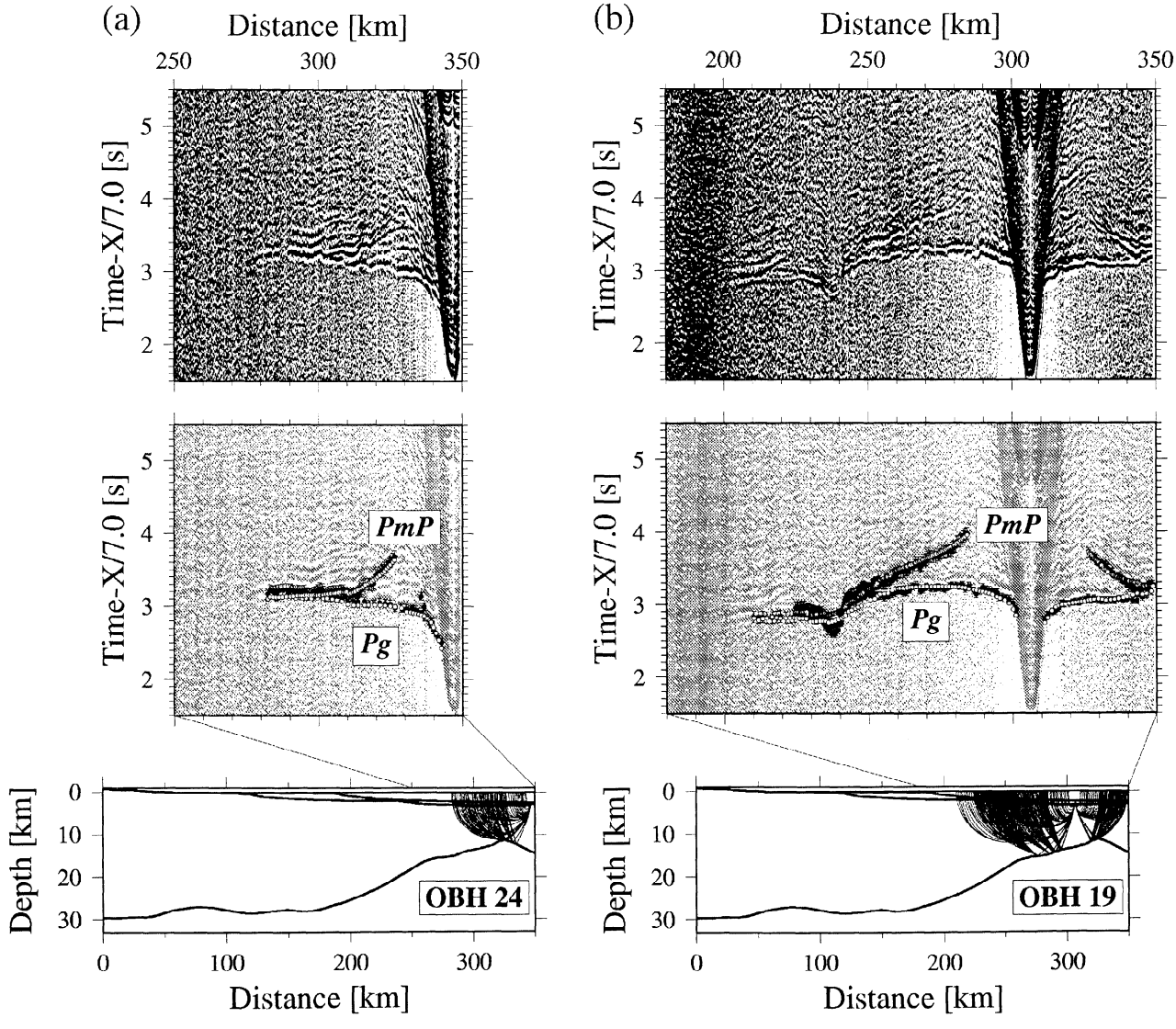

Figure 4. Examples of wide-angle seismic data are plotted after range gain correction, with picked (solid circle with pick error) and predicted (open circle) travel times for *Pg* and *PmP* phases. Synthetic travel times are based on the velocity model presented in Plate 3a, and corresponding ray paths are also plotted at the bottom. (a) OBH 24, (b) OBH 19, (c) OBS A4, (d) OBS C4, (e) OBS C3, (f) OBH 25, (g) OBH 20, (h) ST 18, and (i) ST 15. The 70-s shot data are shown for most of the deep-water and on-land instruments. For the USGS OBS data we show the hydrophone component, which has better quality than the geophone components. Complete data plotting is given by *Korenaga* [2000].

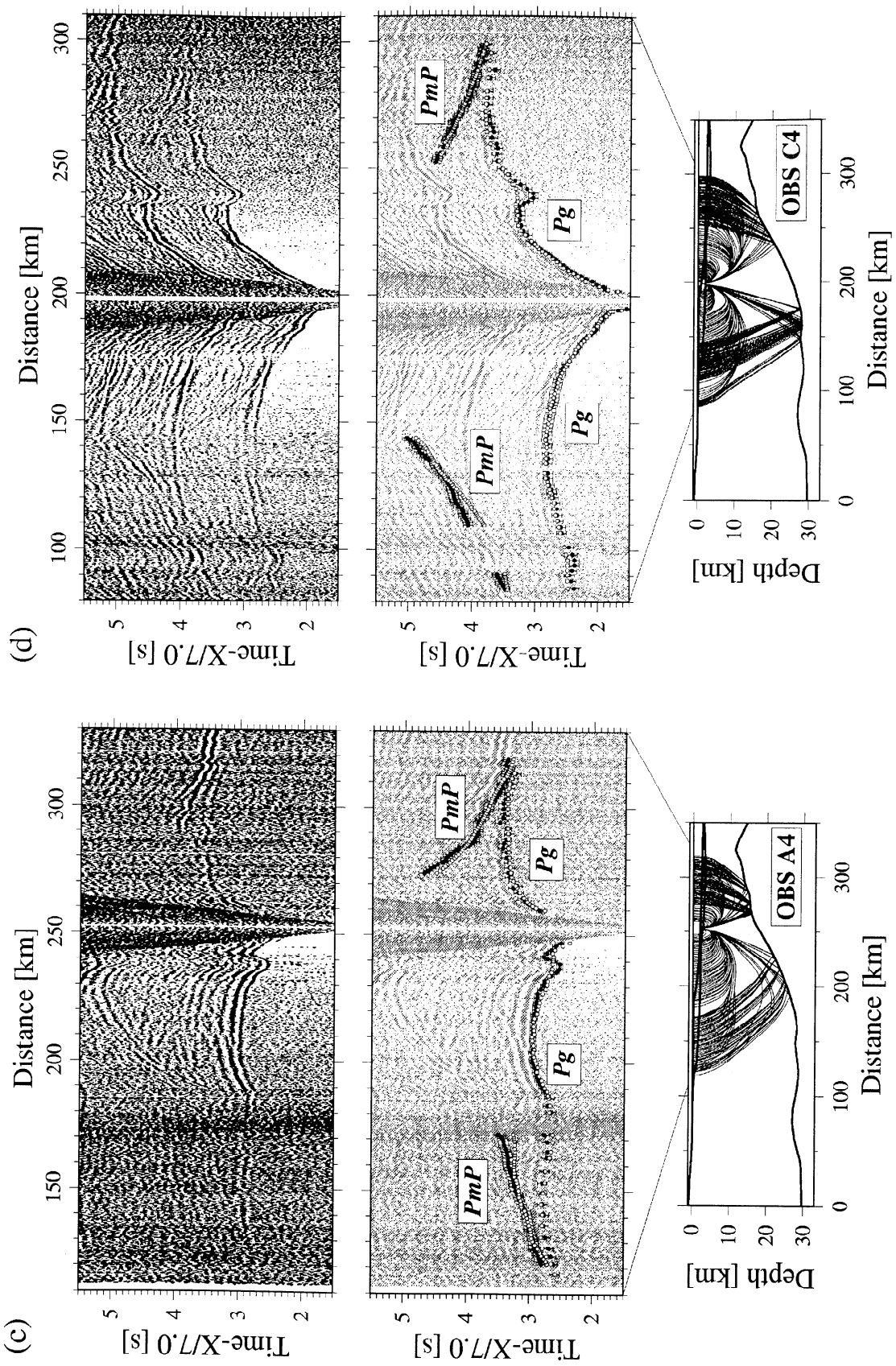

Figure 4. (continued)

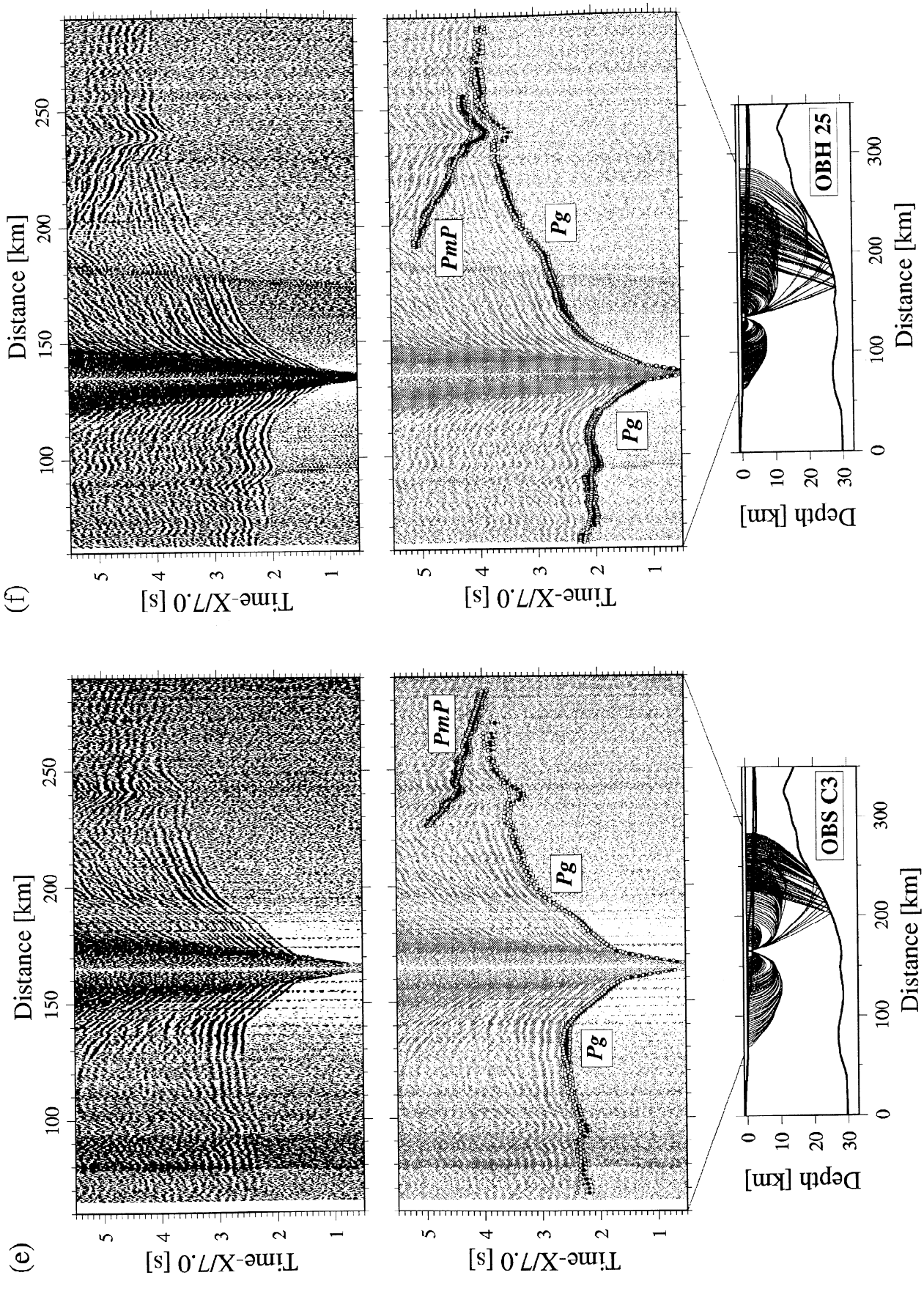

Figure 4. (continued)

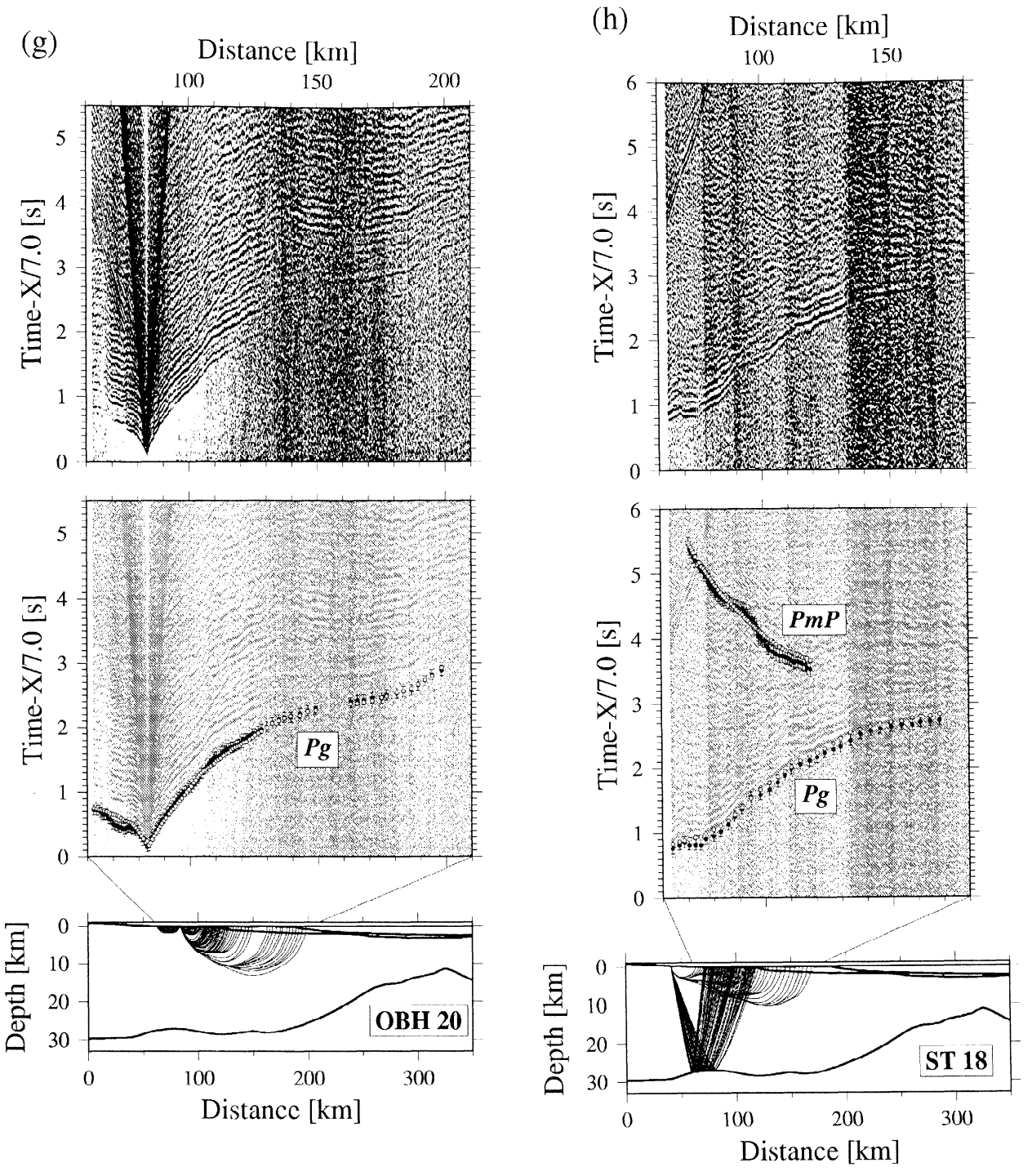

Figure 4. (continued)

network theory [e.g., *Dijkstra*, 1959; *Gallo and Pallottino*, 1986], and it can calculate the shortest connections from an origin node to all other nodes in a network. If a seismic travel time between nodes is used as a nodal distance, this global optimization scheme can be used to generate a set of first-arrival travel times and corresponding ray paths [*Nakanishi and Yamaguchi*, 1986; *Moser*, 1991], and it has recently become popular in refraction tomography [*Toomey et al.*, 1994; *Zhang and Toksöz*, 1998]. The calculation of later arrivals such as reflection phases can be formulated as a two-step application of the graph method [*Moser*, 1991], and it has been used in refraction and reflection tomography [*Zhang et al.*, 1998].

One drawback of the graph method is that the representation of a ray path is restricted by a forward star, which defines the structure of possible node connections [*Matarese*, 1993; *Van Avendonk*, 1998; *Zhang and Toksöz*, 1998]. In a graph solution, therefore, seismic rays tend to zigzag, and travel times are often overestimated. Instead of using a higher-order forward star and a finer mesh to improve the accuracy, we use the ray-bending method [*Um and Thurber*, 1987; *Prothero et al.*, 1988; *Moser et*

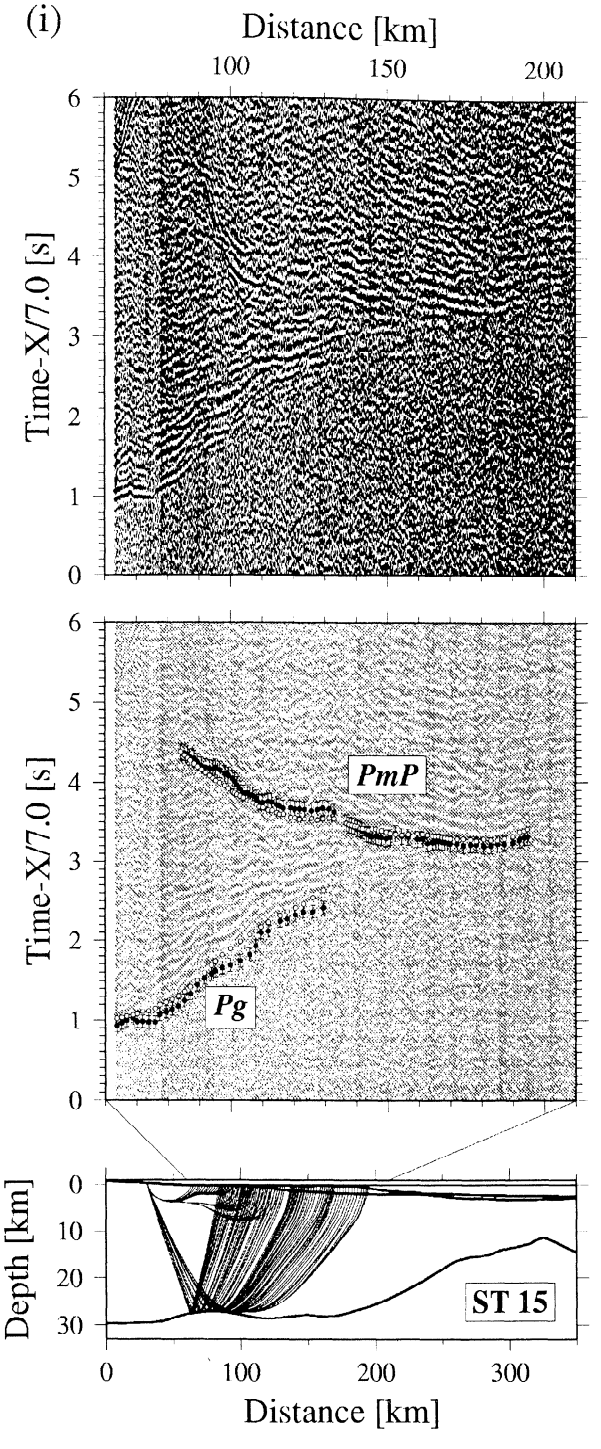

Figure 4. (continued)

al., 1992] to refine a graph solution because we need this extra refinement only for a small portion of node connections in an entire network, i.e., actual source-receiver pairs used in a seismic experiment. A graph solution serves as a good initial guess, which is required for the ray-bending refinement to converge to the global minimum. The finite difference method [*Vidale*, 1988] is another type of wave front ray tracing, but it is inaccurate when large velocity contrasts are present and is limited to the regular grid formulation. These disadvantages are especially grave for its application in marine seismic experiments. Readers are referred to *Zhang* [1997] for an in-depth discussion of a various type of finite difference methods and graph methods in terms of accuracy and efficiency

The ray-bending method can converge more rapidly if a better initial guess is given, so that there is a trade-off between computation times used in the graph method and the bending method. The graph solution with a higher-order forward star provides a better solution with extra computation time, and the order of the forward star that is optimal for this hybrid calculation depends on the node spacing of a velocity model and its complexity. We also note that for a typical crustal velocity model in which the vertical velocity gradient dominates the horizontal one, a forward star that preferentially searches the downward direction is superior to an isotropic forward star with the same number of nodes [*Van Avendonk*, 1998; H. J. A. Van Avendonk et al., Error estimates for the shortest path method and ray bending for traveltime tomography applications, submitted to *Geophysics*, 1999]. In our case, we found that a mixed fifth/tenth order forward star is sufficient for a rapid convergence in the bending refinement. Because the water column is outside the sheared mesh representation of a velocity model, a graph solution would be incomplete without supplying connections between marine sources and seafloor nodes. By Fermat's principle an entry point for a ray starting from a particular marine source can be found by searching all seafloor nodes for a connection with the minimum travel time [e.g., *Toomey et al.*, 1994].

We then apply the ray-bending procedure developed by *Moser et al.* [1992], which employs the conjugate gradient method to directly minimize the travel time along a ray path. Rays are parameterized as beta splines, which can express a variety of curves with a small number of control points, thereby enhancing the convergence in a conjugate gradient search. The nodes used in a graph solution are used as initial control points for beta splines, with an optional dissection for too a long ray segment resulting from the use of a high-order forward star. A constrained conjugate gradient search is used to handle interfaces such as seafloor and a reflector [*Moser et al.*, 1992].

Figure 5 shows an example from the benchmark tests of our ray tracing code. A one-dimensional (1-D) velocity profile representing a typical oceanic crust is used in this example. Analytical ray paths and travel times are calculated based on ray theory [e.g., *Aki and Richards*, 1980]. Three types of numerical ray tracing are compared: (1) the graph method with a velocity grid of 1×0.25 km cells, (2) the graph method followed by the ray-bending refinement, with the same velocity grid, and (3) the graph method with a velocity grid of 0.25×0.125 km cells. Errors in travel time and ray path are summarized in Figures 5g-5j. In the purely graph method applications, the ray path error is bounded by the characteristic spacing of the velocity model, but the travel time error exceeds the target accuracy of 1 ms, which is achieved in the succeeding application of the bending method. Though the pure graph method with a finer grid can be as accurate as the hybrid method, it takes more than 10 times more computation time in this example. Because the computation time used in the bending method is proportional to the number of rays, the computational efficiency will change with a different experiment geometry. On the basis of our experience with a variety of bench mark tests, however, the hybrid approach appears to be generally more compact both in memory and computation time for typical experimental configurations employed in crustal seismology.

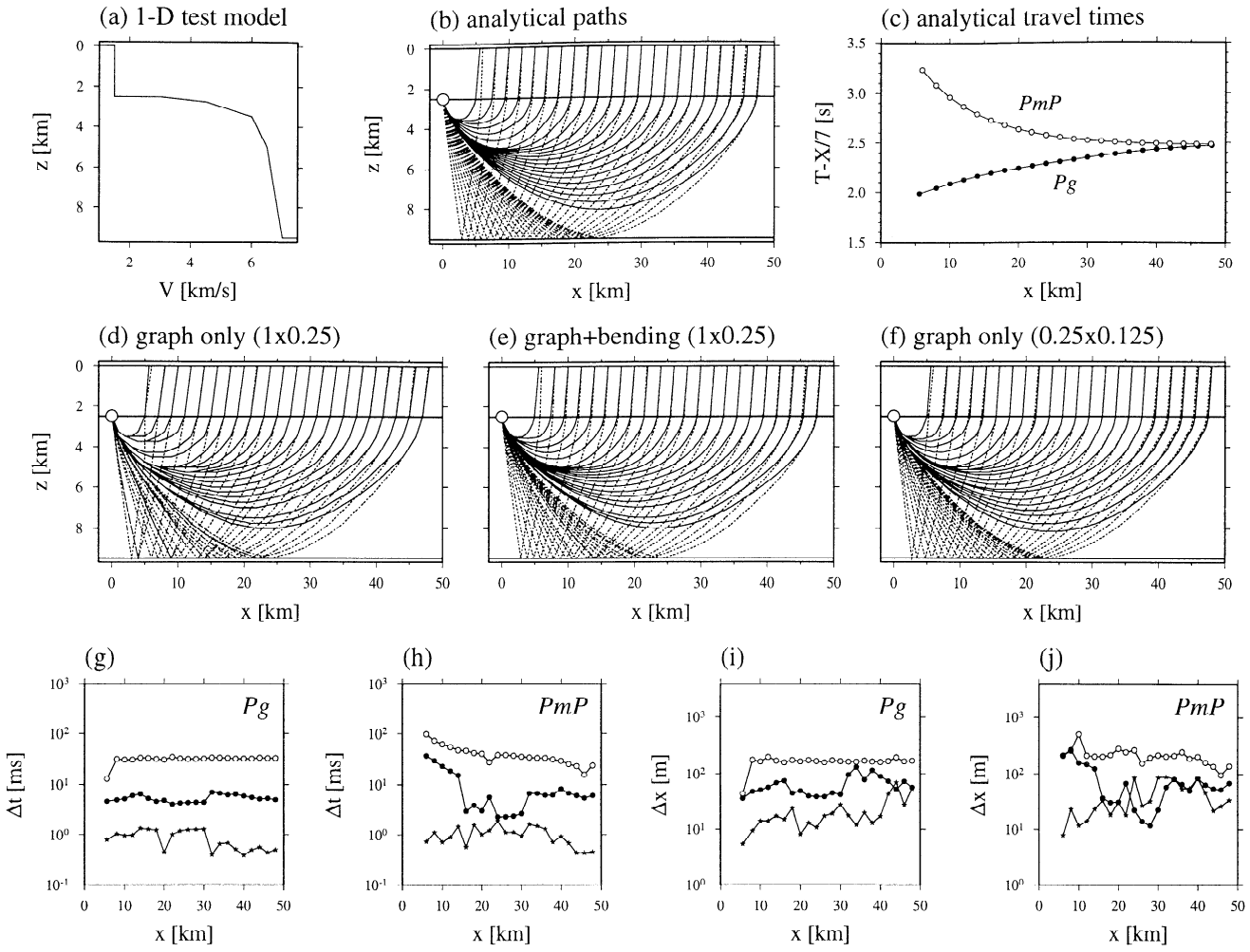

Figure 5. Bench mark test of the ray-tracing algorithm. (a) A 1-D velocity model of typical oceanic crust. (b) Ray paths and (c) travel times calculated for the model using analytical integration for both refraction and reflection phases. Receiver is located on seafloor, and sources are located on the sea surface at ~2-km interval. (d) Ray paths by the graph method with a velocity grid of 1-km horizontal spacing and 0.25-km vertical spacing. (e) Ray paths refined by the ray-bending method. (f) Another purely graph-theoretical paths with a velocity grid of 0.25-km horizontal spacing and 0.125-km vertical spacing. Error in travel times plotted as a function of source-receiver offset in (g) for refraction and (h) for reflection. Open circle, solid star, and solid circle correspond to the pure graph solution (Figure 5d), the hybrid solution (Figure 5e), and the pure graph solution with the finer grid, respectively. Ray dissimilarity plotted in the same way in (i) for refraction and (j) for reflection. Ray dissimilarity is a measure of ray path misfit [e.g., *Fischer and Lees*, 1993], and our definition here is $\Delta x = \int |\mathbf{x}(s) - \mathbf{x}_{\text{true}}(s)|\, ds$, where $\mathbf{x}$ and $\mathbf{x}_{\text{true}}$ are numerical and analytical ray paths, respectively, as a function of the normalized path coordinate, s, defined along each ray.

3.3. Inverse Problem

Given an initial reference velocity model, refraction travel time residuals δT_j can be mapped into slowness perturbations δu along the ray paths Γ_j in a reference model, using the following path integral:

$$\delta T_j = \int_{\Gamma_j} \delta u \, d\Gamma . \tag{1}$$

Similarly, reflection travel time residuals can be written in the 2-D Cartesian coordinates as

$$\delta T_j = \int_{\Gamma_j} \delta u \, d\Gamma + \left.\frac{\partial T}{\partial z}\right|_{x=x_j} \delta z(x_j), \tag{2}$$

where x_j is the reflecting point of the jth ray. By the finite dimensional approximation of velocity and reflector models, equations (1) and (2) can be written collectively as

$$\mathbf{d} = \mathbf{G}\delta\mathbf{m}, \tag{3}$$

where $\mathbf{d}$ is the travel time residual vector, $\mathbf{G}$ is the Fréchet derivative matrix, and $\delta\mathbf{m}$ is the unknown model perturbation vector. This matrix equation forms the foundation of our travel time tomography. The velocity sensitivity part of the Fréchet matrix is simply a path length distributed to relevant velocity nodes according to the bilinear interpolation used for slowness interpolation. The depth sensitivity part can be expressed using an incident angle upon reflection, the slope of a reference reflector, and the velocity at the reflecting point as derived by *Bishop et al.* [1985]. When a starting model is far from the true

model, the above linearized inversion must be applied iteratively until the model converges.

The uncertainty of observed travel times is usually nonuniform, and it can be expressed in the data covariance matrix $\mathbf{C}_d$. Though errors in hand-picked travel times can be correlated to some extent, no correlation in data error is assumed in $\mathbf{C}_d$ for simplicity. This simplified representation of data error does not pose a major problem because we use our iterative inversion merely as an efficient solution finder and will quantify the model covariance by the nonlinear Monte Carlo method. For a controlled-source experiment in crustal seismology, there is often no significant a priori information available for the velocity structure of a study area, so the use of the a priori model covariance matrix is highly limited. Nonetheless, the normalization of model parameters is beneficial to minimize a possible solution bias due to the magnitude of reference model parameters [e.g., *Toomey et al.*, 1994]. Equation (3) is thus normalized through the following relations:

$$\begin{aligned} \mathbf{G}' &= \mathbf{C}_d^{-1/2}\mathbf{G}\mathbf{C}_m^{-1/2}, \\ \delta\mathbf{m}' &= \mathbf{C}_m^{-1/2}\delta\mathbf{m}, \\ \mathbf{d}' &= \mathbf{C}_d^{-1/2}\mathbf{d}, \end{aligned} \tag{4}$$

where the model scaling matrix $\mathbf{C}_m$ is a diagonal matrix whose elements are each a square of a model parameter. Primes will be dropped hereafter, and this normalization is always assumed.

With the typical resolving power of observed travel time data, a fine model parameterization prohibits inversion of equation (3) in its simplest form because of severe singularity, and we need to regularize the linear system to stabilize the inversion. In the absence of a priori information on the scale of velocity variations, the only reasonable way appears to be to restrict the model space with some arbitrary additional constraints [cf. *Scales and Snieder*, 1997]. We choose to apply smoothness constraints on both velocity and depth perturbations using predefined correlation lengths. Because a fully 2-D smoothing constraint on velocity perturbations results in a rather dense matrix that requires large memory storage, we use two 1-D smoothing constraints, one each for horizontal and vertical directions [*Toomey et al.*, 1994]. A regularized linear system can then be written as

$$\begin{bmatrix} \mathbf{d} \\ \mathbf{0} \\ \mathbf{0} \\ \mathbf{0} \end{bmatrix} = \begin{bmatrix} \mathbf{G}_v & w\mathbf{G}_d \\ \lambda_v\mathbf{L}_{\mathrm{H}v} & \mathbf{0} \\ \lambda_v\mathbf{L}_{\mathrm{V}v} & \mathbf{0} \\ \mathbf{0} & w\lambda_d\mathbf{L}_d \end{bmatrix} \begin{bmatrix} \delta\mathbf{m}_v \\ \frac{1}{w}\delta\mathbf{m}_d \end{bmatrix}, \tag{5}$$

where subscripts v and d for the Fréchet matrix and the model vector denote their velocity and depth components, respectively, and where λ_v and λ_d control the relative importance of the smoothing constraints with respect to the data resolution. $\mathbf{L}_{\mathrm{H}v}$ and $\mathbf{L}_{\mathrm{V}v}$ are the horizontal and vertical smoothing matrices for slowness perturbations, respectively, and $\mathbf{L}_d$ is the smoothing matrix for depth perturbations. The depth kernel weighting parameter, w, adjusts the relative weighting of depth sensitivity in the Fréchet matrix. Gaussian smoothing within one decay length is used in all smoothing matrices [e.g., *Toomey et al.*, 1994], which are also normalized by the model scaling matrix to be consistent with the normalization of the Fréchet matrix. To reduce bias toward a starting model, the above formulation contains no information about a reference model except through the model normalization. When a reliable reference model is independently available, however, it is straightforward to modify equation (5) to incorporate a pure jumping strategy [*Shaw and Orcutt*, 1985; *Toomey et al.*, 1994].

Equation (5) is a sparse system so it can be efficiently solved by the sparse matrix solver LSQR [*Paige and Saunders*, 1982]. The computation time used in solving one matrix equation is typically an order of magnitude less than that used for the forward ray tracing. When a starting model is far from a true solution, model updates can be so large that the succeeding iterations become unstable. To avoid this instability, when there are data with too large residuals, we repeat the inversion without the outliers. In addition, damping constraints for velocity and depth nodes are added to equation (5):

$$\begin{bmatrix} \mathbf{d} \\ \mathbf{0} \\ \mathbf{0} \\ \mathbf{0} \\ \mathbf{0} \\ \mathbf{0} \end{bmatrix} = \begin{bmatrix} \mathbf{G}_v & w\mathbf{G}_d \\ \lambda_v\mathbf{L}_{\mathrm{H}v} & \mathbf{0} \\ \lambda_v\mathbf{L}_{\mathrm{V}v} & \mathbf{0} \\ \mathbf{0} & w\lambda_d\mathbf{L}_d \\ \alpha_v\mathbf{D}_v & \mathbf{0} \\ \mathbf{0} & w\alpha_v\mathbf{D}_d \end{bmatrix} \begin{bmatrix} \delta\mathbf{m}_v \\ \frac{1}{w}\delta\mathbf{m}_d \end{bmatrix}, \tag{6}$$

where $\mathbf{D}_v$ and $\mathbf{D}_d$ are the damping matrices for velocity and depth nodes, respectively, constructed in a manner similar to that of *Van Avendonk et al.* [1998], and α_v and α_d control the strength of the damping constraints. Therefore there are four weighting parameters in total in our inverse equation: two for smoothing and two for damping. Even though solving a single sparse system is computationally inexpensive, trying to find the optimal combination of the four parameters to satisfy some user-defined constraints such as desired model roughness requires a number of trial solutions at each iteration, which we regard as impractical. Our strategy is to first determine the smoothing weights by systematically testing velocity and depth smoothing with a preliminary single-step inversion and then to fix these weights throughout all subsequent iterations. When model perturbations are found to be too large, optional sweeps on the damping weights are done by the secant and bisection method to satisfy user-defined upper limits on average velocity and depth perturbations. In the later phase of iterations, model perturbations tend to become very small, and weak, but undesired model roughness can emerge with this fixed smoothing strategy. To amend this, postinversion smoothing is applied at each iteration as

$$\mathbf{m}_{i+1} = \mathbf{m}_i\,(1+\mathbf{L}_v(\delta\mathbf{m}_i) - \delta\mathbf{m}_c), \tag{7}$$

where $\mathbf{L}_v$ denotes the 2-D smoothing operator for velocity parameters, $\delta\mathbf{m}_i$ is the ith model update, and $\mathbf{m}_i$ and $\mathbf{m}_{i+1}$ are the ith and $(i+1)$th model solutions, respectively. The parameter $\delta\mathbf{m}_c$ is a correction term to conserve data resolution during the a posteriori filtering [*Deal and Nolet*, 1996], and it is calculated by solving

$$\mathbf{G}\delta\mathbf{m}_c = \mathbf{G}(\mathbf{L}_v(\delta\mathbf{m}_i) - \delta\mathbf{m}_i). \tag{8}$$

As well as compensating our compromise of using 1-D smoothing matrices in equation (5), this 2-D smoothing ensures model convergence with given correlation lengths.

A major concern in reflection tomography is the existence of nonuniqueness regarding the depth of a reflector and the velocity above it. Even in our joint refraction and reflection tomography, this nonuniqueness can still be present because the lower crustal velocity is mainly resolved only by reflection travel times. There are a number of theoretical studies on the nature of this velocity-depth ambiguity [e.g., *Bickel*, 1990; *Stork*, 1992a, 1992b; *Ross*,

1994; *Bube et al.*, 1995], but their treatments are limited to simple velocity structures and some particular source-receiver configurations. It is probably unrealistic to expect a general theory that can be versatile enough to handle a number of source-receiver pairs with different ray coverage, strongly heterogeneous velocity structure, and variable interface topography. Therefore we propose a practical strategy to investigate the degree of the velocity-depth ambiguity using the depth kernel weighting parameter w in equation (5). Even with smoothness constraints on velocity and depth, the linear system for joint refraction and reflection tomography can still be singular because of this velocity-depth ambiguity. For a singular system, iterative matrix solvers based on conjugate gradients such as LSQR provide the minimum-norm solution if starting with an initial null vector [*Hestenes*, 1975]. The weighting parameter of unity corresponds to the equal weighting of velocity and depth nodes [*Stork and Clayton*, 1991], and increasing the weighting parameter should lead to larger depth perturbations with smaller velocity perturbations if the system is singular. We can thus test the velocity-depth ambiguity by systematically exploring the solution space with the single controlling parameter.

A numerical example to demonstrate this approach is shown in Figure 6. In this example, a starting model already has the true velocity field, but the reflector is located 1 km shallower than the true one. With dense ray coverage as in Figure 6b, the inversion successfully recovers the true reflector location with negligible velocity perturbations, regardless of the value of w (Figures 6c and 6d). When ray coverage is sparse (Figure 6e), the inversion with equal weighting results in an insufficient recovery of the reflector depth with compensating velocity perturbations (Figure 6f), and a desirable recovery can be obtained with greater depth sensitivity (Figure 6g). The travel time fits for the two different recoveries are nearly the same; thus they are indistinguishable from data resolution. The weaker weighting of depth nodes would provide the other end of the valid model space. When there is no other information to discriminate among these different recoveries, one should present all of them as equally legitimate inverse solutions to characterize the velocity-depth ambiguity. The ambiguity is mainly controlled by available ray coverage and the scale of perturbations we want to resolve, and in general it can be reduced by using greater correlation lengths. Correlation lengths for depth nodes therefore must be

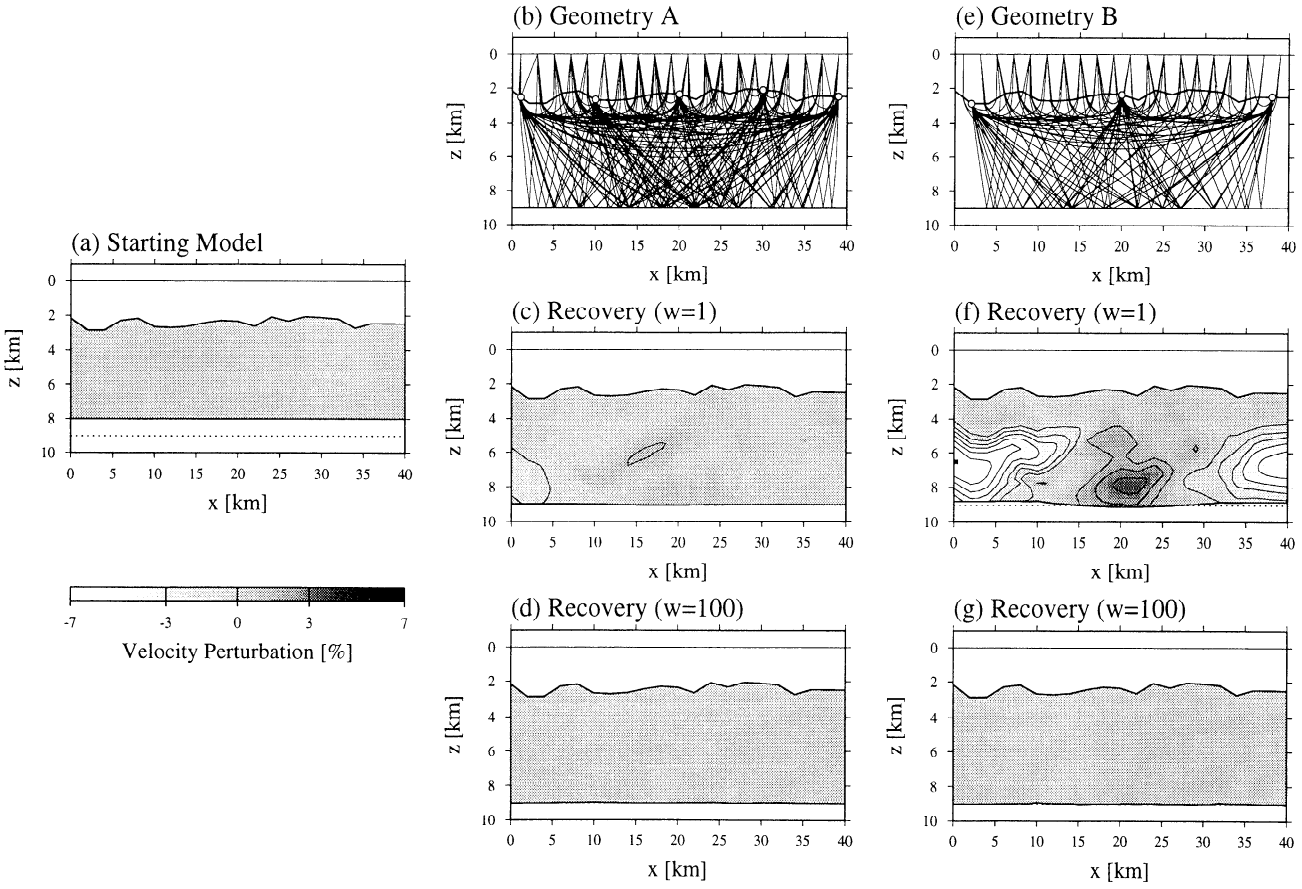

Figure 6. Numerical examples to demonstrate velocity-depth ambiguity in reflection tomography. In a true model, 1-D velocity profile similar to Figure 5a was hung beneath the seafloor, and a reflector is located at depth of 9 km. (a) Starting model with true velocity structure (i.e., no velocity perturbation) but with reflector (solid) located 1-km shallower than true reflector (dotted). Two types of geometry were tested with this starting model. (b) Geometry A with five ocean bottom receivers and 20 sources. Inversion results with (c) w=1 and (d) w=100, both showing excellent recovery. (e) Geometry B with the same sources as geometry A but only three receivers. (f) Recovery with w=1 showing unwanted velocity perturbation and incomplete restoration of the reflector. (g) Higher weighting of depth sensitivity (w=100) resulting in better recovery. The corresponding travel time fits in (Figure 6f) and (Figure 6g) are virtually the same. In all inversions, horizontal correlation length is set as 5 km at the seafloor and 10 km at the model bottom, and vertical correlation length is set as 0.5 km at the seafloor and 1 km at the bottom.

comparable with those for velocity nodes to properly evaluate the extent of the ambiguity.

The above depth kernel weighting should not be confused with weighting reflection data against refraction data. A linear system corresponding to the latter case may be expressed as

$$\begin{bmatrix} \mathbf{d}_1 \\ \alpha\mathbf{d}_2 \\ \mathbf{0} \\ \mathbf{0} \\ \mathbf{0} \end{bmatrix} = \begin{bmatrix} \mathbf{G}_v^1 & \mathbf{0} \\ \alpha\mathbf{G}_v^2 & \alpha\mathbf{G}_d^2 \\ \lambda_v\mathbf{L}_{Hv} & \mathbf{0} \\ \lambda_v\mathbf{L}_{Vv} & \mathbf{0} \\ \mathbf{0} & \lambda_d\mathbf{L}_d \end{bmatrix} \begin{bmatrix} \delta\mathbf{m}_v \\ \delta\mathbf{m}_d \end{bmatrix}, \quad (9)$$

where $\mathbf{d}_1$ and $\mathbf{d}_2$ denotes refraction and reflection travel times, respectively, and α controls the importance of reflection data relative to refraction data. Changing the value of α from unity results in a different linear system, whereas changing the depth kernel parameter w in equation (5) does not. This difference is vital. In addition, the use of equation (9) is not generally recommended because the relative importance between refraction and reflection data should be already incorporated as corresponding data variance.

4. Results of Tomographic Inversion

4.1. Long-Wavelength Structure

From the 25 wide-angle data sets, 2318 *Pg* and 2078 *PmP* travel times were picked to invert for the crustal structure along transect 2. The model domain is 350 km wide and 40 km deep from seafloor. The horizontal grid spacing is ~1 km on average, and the vertical grid spacing gradually increases from 50 m at the seafloor to 1 km at the model bottom, amounting to over 27,000 velocity nodes (Figure 7). The number of reflector nodes is 351 with a uniform 1-km spacing. On the basis of the expected resolving power of our data and a number of preliminary tests on model regularization, we chose to define the correlation length function as follows: the horizontal correlation length for velocity nodes ranges from 10 km at seafloor, linearly increasing to 20 km at the bottom, and the vertical correlation length also varies linearly from 50 m at seafloor to 4 km at the bottom. We have experimented a number of different correlation length functions, and varying these correlation lengths by 50% does not significantly affect the overall smoothness. There is also a trade-off between correlation lengths and smoothing weights, and it is possible to reduce memory requirements by using shorter correlation lengths and larger smoothing weights. The correlation lengths for the reflector nodes are sampled from the 2-D horizontal correlation length function for velocity nodes, using the reflector depths at each iteration. We choose to impose no lateral variation in the correlation length functions to minimize the influence of the prescribed correlation lengths on the structural interpretation of the continent-ocean transition zone.

The sedimentary section was already modeled with MCS vertical-incident travel times and wide-angle basement reflection travel times as reported by Holbrook et al. (submitted manuscript, 2000) and it is incorporated in a starting model as the a priori information. We prepared a starting model for the crustal part by smoothing the preliminary crustal model of Holbrook et al., which was constructed using the semiforward modeling approach of *Zelt and Smith* [1992], with a 100-km-wide and 10-km-high Gaussian window (Plate 1a). The initial root-mean-square (RMS) travel time misfit is 137 ms, with χ^2 of 3.60. Average model perturbations at each iteration were <2% for both velocity and depth throughout the inversion, so no damping was applied. After 10 iterations, model perturbations became ~0.05% for velocity and ~0.1% for depth, and the RMS travel time misfit was reduced to 77 ms with χ^2 of 1.02 (Plate 1b).

Three distinct types of crust can be identified in the final model: (1) ~30-km-thick continental crust near the landward end of the transect, (2) 30- to 15-km-thick transition zone crust from km 100 to 250, and (3) 15- to 9-km-thick oceanic crust from km 250 to the seaward end. The velocity of continental crust ranges almost linearly from 6.0 km/s at the surface to 7.2 km at 30 km depth, which closely resembles the global average velocity profile for continental crust [*Christensen and Mooney*, 1995]. A high-velocity-gradient upper crust appears from km 60, with this transition from low-velocity-gradient to high-velocity-gradient upper crust tentatively interpreted as the continent-ocean boundary. This continent-ocean boundary at shallow crustal levels roughly coincides with the mapped coast-parallel dike swarm [e.g., *Larsen and Duncan*, 1996]. The transition zone crust has ~6-km-thick upper crust, and the bottom half of its lower crust has a velocity exceeding 7.0 km/s. From km 100 to 150 the high-velocity lower crust is thickened, producing a good contrast to the lower-velocity continental crust. Although the lower crustal velocity of the transition zone crust becomes higher toward the Moho than that of normal oceanic crust (~6.9 km/s) [*White et al.*, 1992], we note that it is not quite as high as those

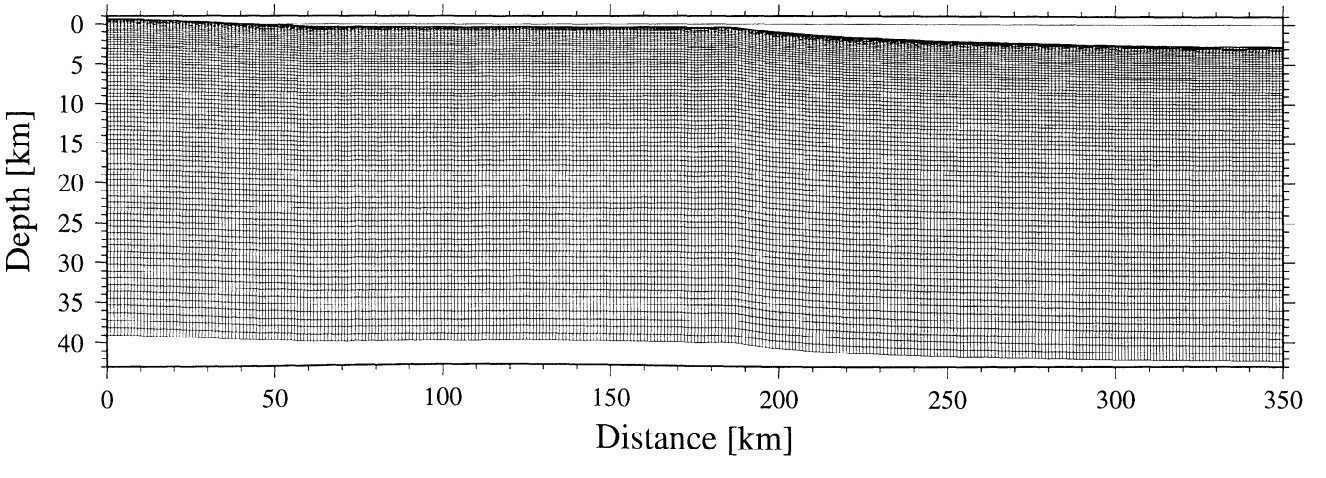

Figure 7. A velocity mesh is composed of 351×77 variable size cells hanging from seafloor.

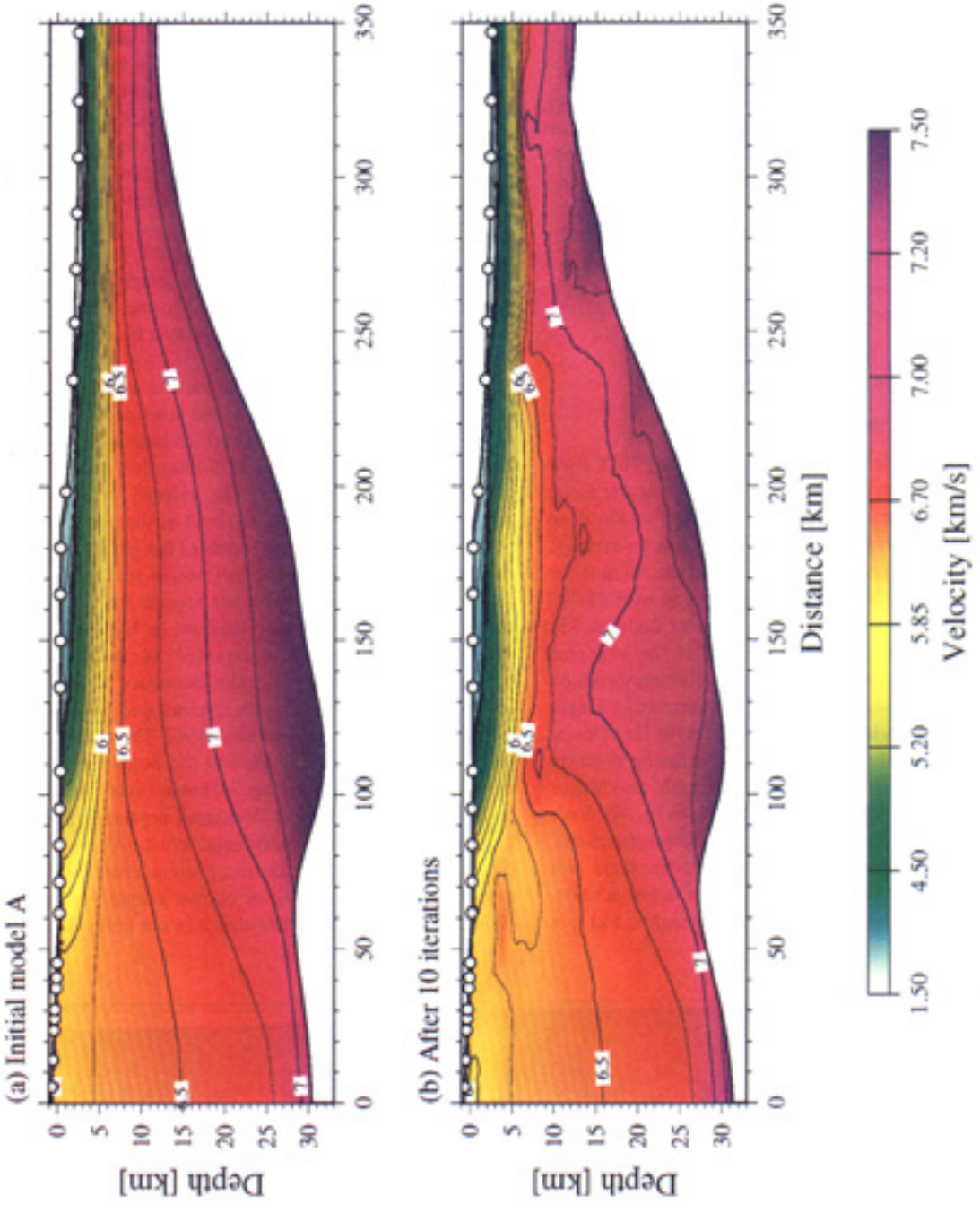

Plate 1. Result of tomographic inversion. (a) Initial model constructed by filtering the preliminary model reported by Holbrook et al.(submitted manuscript, 2000). Gaussian filtering with horizontal window of 100 km and vertical window of 10 km was applied. (b) After 10 iterations, RMS travel time misfit was reduced to 77 ms with χ^2 of 1.02.

found in other seismic transects on North Atlantic margins [*White et al.*, 1987; *Mutter and Zehnder*, 1988], which are higher than 7.2 km/s for most of the lower crust. The thickness of the upper crust reduces to ~3 km for the oceanic crust. Though this part of the crust is thinnest along the transect, it is still thicker than normal oceanic crust with 6 to 7 km thickness [*White et al.*, 1992]. Its velocity is still higher than 7.0 km/s in the bottom half of the lower crust, and a prominent high-velocity anomaly is observed near the Moho from km 260 to 300.

To examine the sensitivity to starting models, we conducted another set of inversions with a different starting model. The second starting model was constructed by hanging a 1-D average crustal velocity profile calculated from Plate 1a beneath the basement, and the initial Moho was set flat at 25 km deep (Plate 2a). The initial RMS travel time misfit exceeded 800 ms with χ^2 of 136.1, but outliers with normalized residuals >5 after the first iteration are only 2.3% of all data, indicating a minor role of outlier removal. Damping was applied to retain average slowness and depth perturbations below 3% and 9%, respectively. After the first two iterations, damping was no longer required, and all the travel time residuals were within the cutoff threshold. After 10 iterations the RMS travel time misfit reduced to 78 ms with χ^2 of 1.01 (Plate 2b). Though the details differ, the main key structural features observed in Plate 1b remain the same. These features include the overall variation in crustal thickness, the thickening of the high-velocity-gradient upper crust from the seaward end to the continental shelf, and its sudden thinning near the coast line. The crustal velocity structure from km 170 to 330, including the small-scale high-velocity anomaly in the lower crust around km 280, is almost identical between the two models, indicating that this part of the model is well resolved and virtually independent of starting models. An increase in the lower crustal velocity at km 100 to 150 is also found in the second model, though its overall velocity is lower. A majority of the continental crust seems to require an average velocity of ~6.5 km/s with an almost linear velocity gradient, as found in both models. These close similarities between the two models satisfactorily demonstrate the robustness of the resolved velocity structure.

To investigate the degree of velocity-depth ambiguity in our inversion, we repeated the inversion with the starting model of Plate 1a, using two different values, 0.01 and 100, for depth kernel weighting. The inversion solutions after 10 iterations are shown in Figure 8 along with the solution for equal weighting. The travel time misfits for the three models are very similar. Since there is no major difference found among these models, we conclude that our inversion solution does not suffer from serious velocity-depth ambiguity, given the relatively wide spatial correlation that we employed in the smoothing constraints. We will thus employ the equal weighting of the velocity and depth kernels in all the following inversions.

4.2. Resolution and Accuracy

The ray coverage in the model can be concisely represented by the derivative weight sum (DWS) [*Toomey and Foulger*, 1989], which is the column-sum vector of the Fréchet velocity kernel. The DWS for our velocity model is shown in Figure 9, as a crude measure of the linear sensitivity in our inversion. The lower crust at km 30 to 130 is sparsely covered by reflections alone, implying lower resolution than the other parts of the model.

Because the DWS does not provide any quantitative information regarding the resolution and accuracy of the model and because nonlinear sensitivity is important for iterative inversions [e.g., *Zhang and Toksöz*, 1998], we conduct two types of analyses: (1) resolution tests using synthetic data and (2) a nonlinear Monte Carlo uncertainty analysis. In the resolution tests we calculate synthetic data for a perturbed velocity model with the same sources and receivers as in the actual observation, add random noise of 100 ms to the synthetic data, and invert them with an initial unperturbed model to see how well given perturbations are recovered. Though not comprehensive, this is a succinct and computationally inexpensive way to demonstrate the resolving power of the available ray coverage. In the first resolution test we perturbed velocity nodes with 5% positive and negative anomalies of a 140-km wavelength aligned in the midcrust (Figure 10a). Good recovery was obtained for the seaward half of the model (Figure 10b). Despite a significant deterioration toward the landward end, the result suggests that the ray coverage of our data is sufficient to resolve the continent-ocean boundary around km 100. The recovered anomalies tend to be laterally stretched, resulting from our conservative choice of the horizontal correlation length. In the second resolution test, only the reflector nodes were perturbed with a 1.5-km amplitude and a 100-km wavelength (Figure 10c). The perturbed Moho was well recovered for km 50 to 100 and km 150 to 330. The parts that were not recovered correctly, such as km 100 to 150 and near the model ends, are indeed poorly sampled by *PmP* (Figure 9). The unrecovered reflector perturbations leak into velocity perturbations above the reflector, but their amplitude is only ~0.5%, being consistent with the negligible velocity-depth ambiguity indicated in Figure 8.

The uncertainty of the seismic velocity is fundamental for the reliable interpretation of crustal composition. The only practical way to estimate the model uncertainty for a large-scale, nonlinear inversion such as our tomography is the Monte Carlo method [e.g., *Tarantola and Valette*, 1982; *Tarantola*, 1987]. By inverting data with random errors with random initial models, we can construct a number of Monte Carlo realizations, with which the a posteriori model covariance matrix is estimated as

$$\mathbf{C} = \int [\mathbf{p} - E(\mathbf{p})] \cdot [\mathbf{p} - E(\mathbf{p})]^{\mathrm{T}} \sigma_{\mathbf{p}}(\mathbf{p}) d\mathbf{p}, \tag{10}$$

where $\mathbf{p}$ is the solution vector of the realizations, $E(\mathbf{p})$ is the a posteriori expectation of $\mathbf{p}$, and $\sigma_{\mathbf{p}}(\mathbf{p})$ is the a posteriori marginal density function [*Tarantola and Valette*, 1982]. By assuming that all N realizations have the same probability, we may approximate the above definition as [*Matarese*, 1993]

$$\mathbf{C} \approx \frac{1}{N} \sum_{i=1}^{N} [\mathbf{p}_i - E(\mathbf{p})] \cdot [\mathbf{p}_i - E(\mathbf{p})]^{\mathrm{T}}, \tag{11}$$

where $\mathbf{p}_i$ is the solution of the ith realization. *Zhang and Toksöz* [1998] noted that modeling data errors with Gaussian errors for absolute travel times is unrealistic in light of the nature of travel time picking, and they suggested using common shot errors (or common receiver errors in the case of marine experiments) and travel time gradient errors. We thus randomized data by adding the following two error components to the original data: random common receiver errors with a maximum amplitude of 50 ms, and random travel time errors with the same maximum amplitude. The small-amplitude travel time errors have virtually the same function as the travel time gradient errors used by *Zhang and Toksöz* [1998]. The highly correlated nature of travel time pick errors can be taken into account by this data randomization. Random initial velocity models were prepared by hanging random 1-D crustal velocity profiles beneath the basement. A two-layer crustal model was used to generate

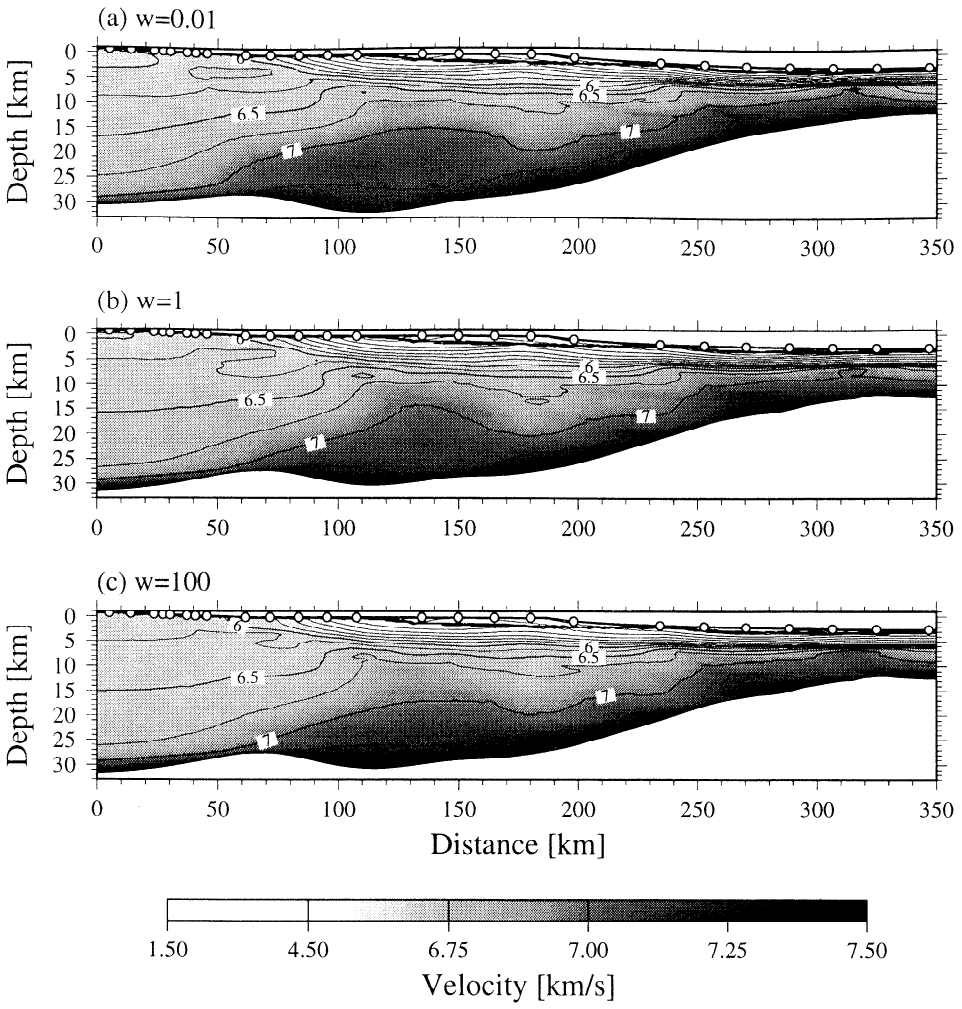

Figure 8. Test of velocity-depth ambiguity using different weighting of the depth kernel. Initial model is shown in Plate 1a and 10 iterations were applied. (a) w=0.01, (b) w=1 (samc as Platc 1b), and (c) w=100. RMS travel time misfits are 78, 77, and 77 ms, respectively.

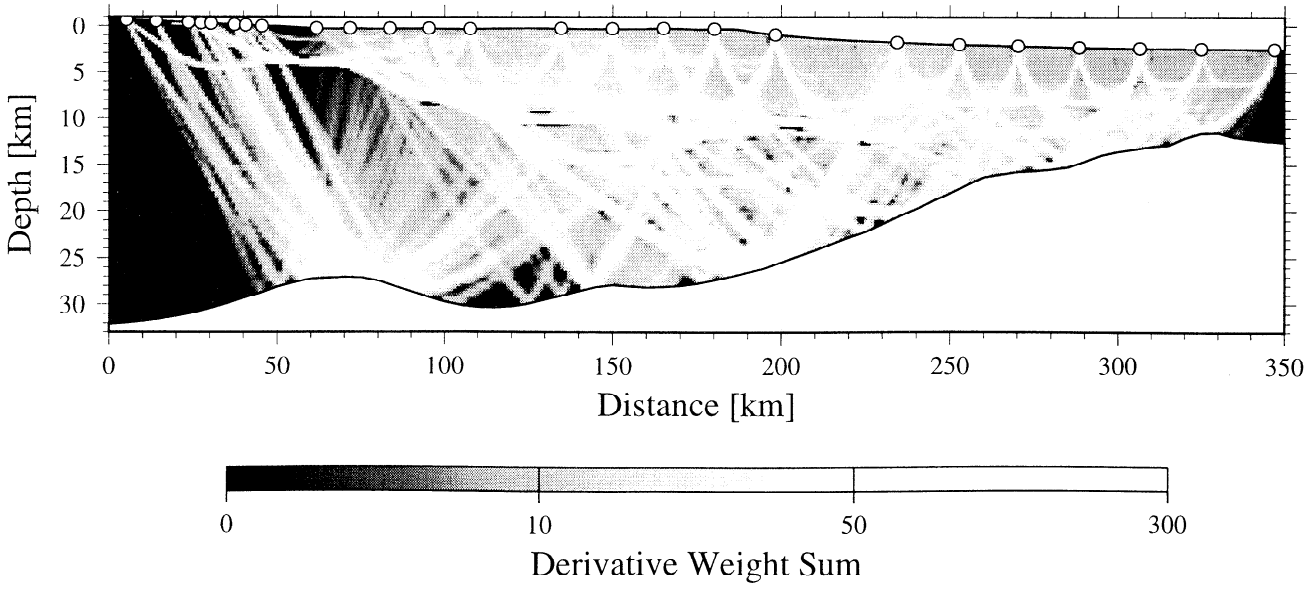

Figure 9. Derivative weight sum in the case of the solution shown in Plate 1b.

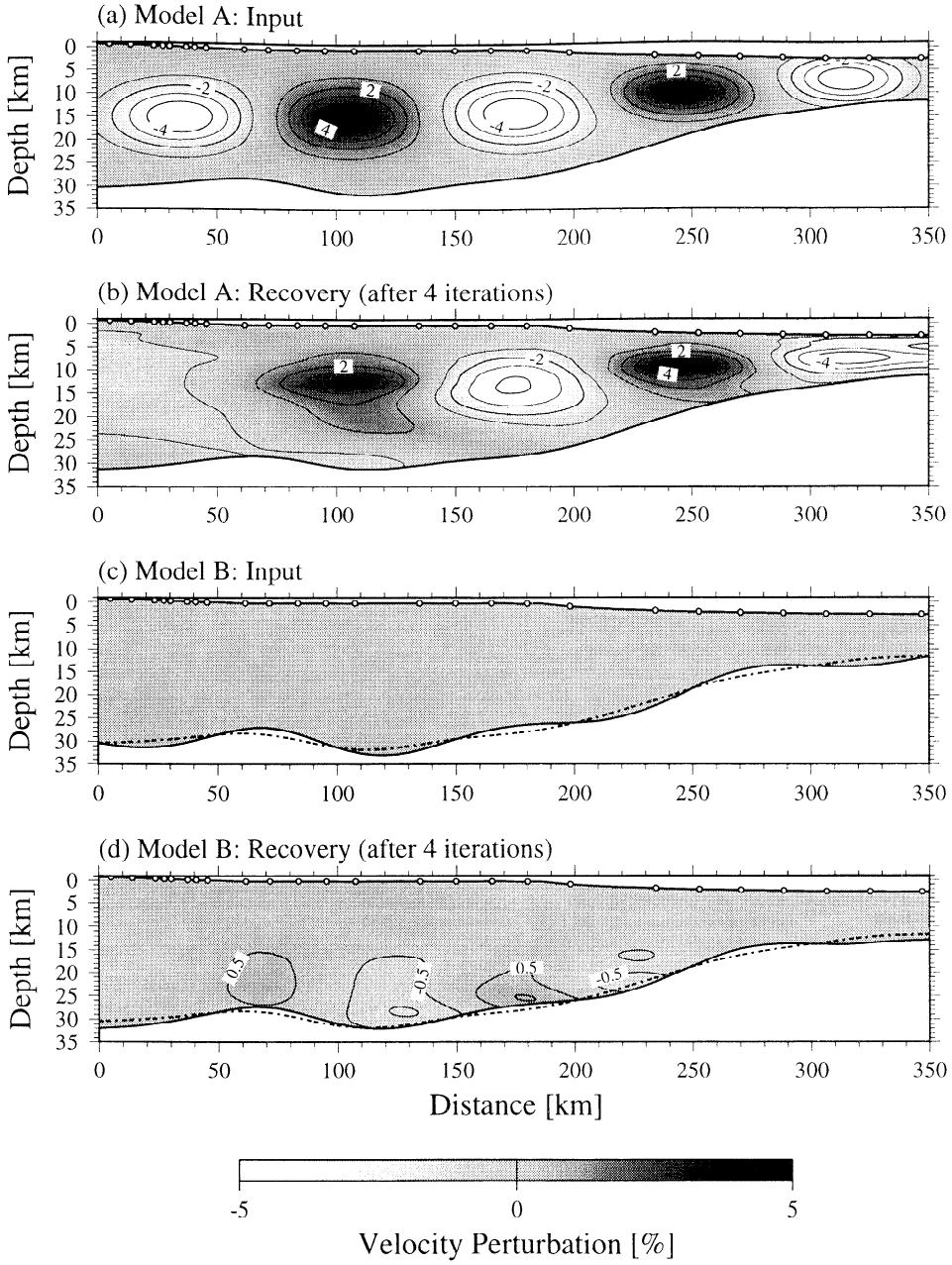

Figure 10. Resolution tests. Reference velocity model is the same as in Plate 1a. We use the same source and receiver locations for synthetic travel time calculation, and random noise of 100 ms was added to synthetic data prior to inversion. (a) True model perturbation consisting five alternating 5% velocity anomalies. (b) Recovery obtained after four iterations. Almost no change is observed for reflector depths. (c) Model reflector (solid) constructed by adding 1.5-km perturbation with 100-km wavelength to the reference reflector (dashed). (d) Starting from the reference reflector, good recovery obtained for most parts with small leaking into velocity perturbations.

random 1-D profiles; there are five controlling parameters such as top, midcrustal, and bottom velocities and upper and lower crustal thicknesses, and their possible variations were chosen so to cover a wide range of 1-D crustal velocity profiles (Figure 11). The RMS amplitude of this initial velocity randomization with respect to a typical Monte Carlo ensemble (e.g., Plate 2b) is ~5%. Initial reflector depths were uniform and randomly set between 20 and 30 km, independently with initial crustal velocity profiles. With this degree of model perturbations, normalized χ^2 was generally higher than 100, with an RMS travel time misfit >800 ms. On average, 10 iterations were required to reduce normalized χ^2 to ~1.0. Using 100 realizations, the final crustal velocity model as well as the a posteriori model variance were calculated (Plate 3). The standard deviation of the velocity nodes is lowest (<0.05 km/s) at the midcrust, where most of refraction rays turn (Figure 9). From km 50 to 330, most of the velocity nodes have a standard deviation of less than 0.10 km/s (Plate 3). The standard deviation of the Moho depths is <0.25 km for the thinner crust and ~1.5 km for the thicker crust.

Using the Monte Carlo ensembles, one can estimate the uncertainty of an averaged quantity by applying the averaging operation to each ensemble and then calculating the variance

from the whole averaged ensembles. Even when model parameters have large errors, the variance of their average can be much smaller if the errors are negatively correlated. The above approach using the Monte Carlo realizations correctly handles this parameter correlation. The Monte Carlo ensembles obtained in this section will be used when we discuss the relationship between crustal thickness and average crustal velocity.

5. Discussion

5.1. Short-Wavelength Structure

The travel times predicted by the long-wavelength velocity structure consistently fail to fit the small undulations of ~200 ms in the observed travel times around km 230 to 245 (Figure 4). This negative travel time misfit is found for all the refraction and reflection phases shot from that model range, which coincides with the basement high and the occurrence of the seaward termination of the SDR wedge (Figure 3), so that they must originate in a positive velocity anomaly in a shallow depth below the basement high. To resolve this positive velocity anomaly, we inverted a subset of the travel time data with shorter correlation lengths; the horizontal and vertical correlation lengths were set as 5 km and 0.5 km, respectively, for a 150-km-wide and 10-km-deep subregion including the basement high. After only one iteration we were able to achieve excellent travel time fits (Figure 12a). The high-resolution velocity model shows that a 15-km-wide and 4-km-thick region beneath the basement high has velocities higher by 0.5-1.0 km/s than the adjacent upper crust (Figure 12b).

The shallow positive velocity anomaly provides an important constraint on the origin of the basement high. A similar velocity anomaly identified beneath the Krafla central volcano in Iceland [*Brandsdóttir et al.*, 1997; *Staples et al.*, 1997] has been interpreted as a shallowing of the igneous intrusion depth. The termination of the SDR sequence adjacent to the basement high is consistent with this explanation on the basis of models of SDR evolution [*Hinz*, 1981; *Mutter et al.*, 1982]. In addition, there must have been a small-scale, seaward ridge jump from the eruption center to leave the high-velocity anomaly region within the continental margin crust. The other possibility is that the positive velocity anomaly represents a later intrusion cutting through the preexisting SDRs, as suggested for the "outer high" on the Hatton Bank [*White et al.*, 1987; *Barton and White*, 1997b]. Unlike the case of the Hatton Bank, however, almost no coherent linear structure is observed on the seaward side of the basement high to support this hypothesis (Figure 12c). Moreover, the thickness of the upper crust drastically changes across the basement high (e.g., Plate 1b), further reducing the likelihood that the data can be explained as the result of a later intrusion. An abandoned rifting axis thus appears to be the most likely explanation for the basement high.

5.2. Difference From Previous Work

The compressional velocity model of transect 2 presented by Holbrook et al. (submitted manuscript, 2000) was constructed using the iterative damped least square inversion of *Zelt and Smith* [1992]. The model consists of three layers, i.e., sedimentary, upper crustal, and lower crustal layers, and it is parameterized by a few tens of trapezoidal velocity cells. Its RMS travel time misfit is ~100 ms with χ^2 of ~2.1. Given the simplicity of the model parameterization, this acquired misfit is considered to be reasonable, and the velocity model that we obtained through our new tomography is very similar to this preliminary model.

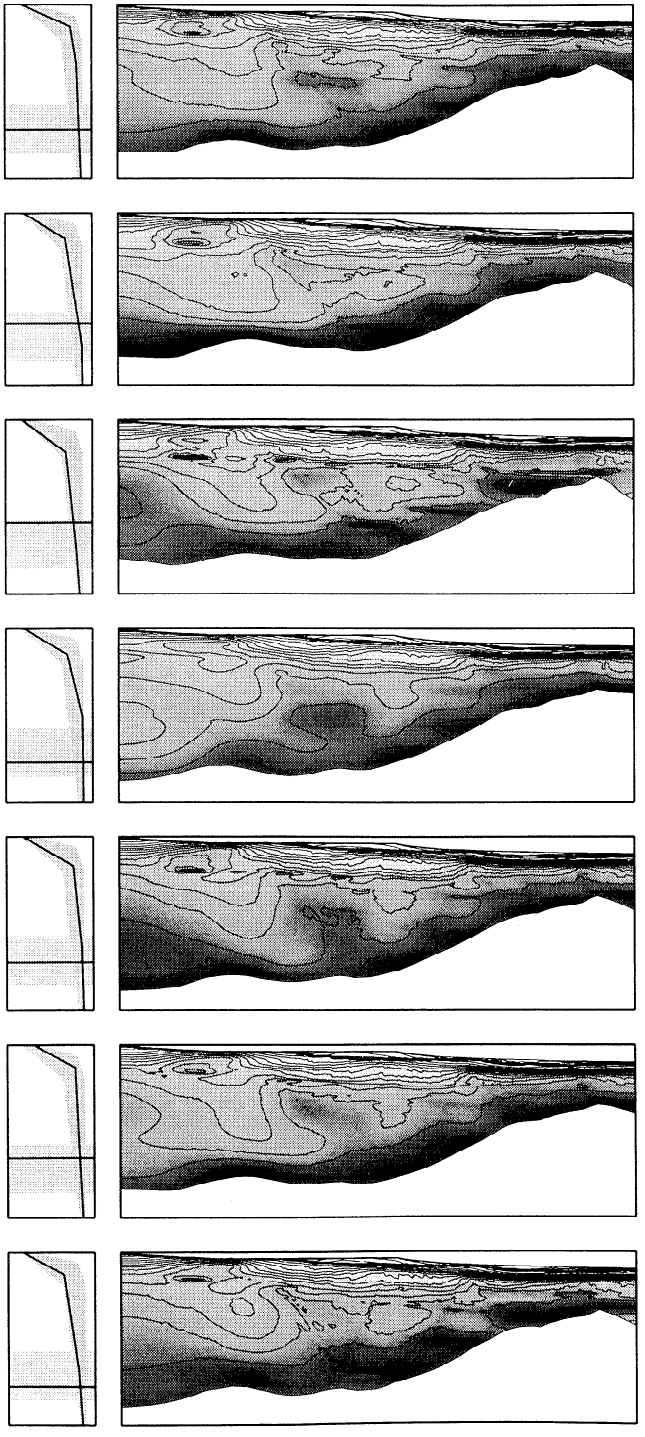

Figure 11. (left) Example of randomized starting models and (right) corresponding Monte Carlo ensembles in the uncertainty analysis. A starting model consists of a 1-D crustal velocity profile and a flat Moho. Gray regions show possible variations in our model randomization. Minimum values for top, midcrustal, and bottom velocities are 3.8, 6.2, and 7.0 km/s, while corresponding maximum values are 4.6, 7.0, and 7.5 km/s, respectively. The upper crustal thickness can vary from 2 to 7 km, and the lower crustal thickness can vary from 5 to 24 km. Initial Moho is flat and randomly set at a depth between 20 and 30 km.

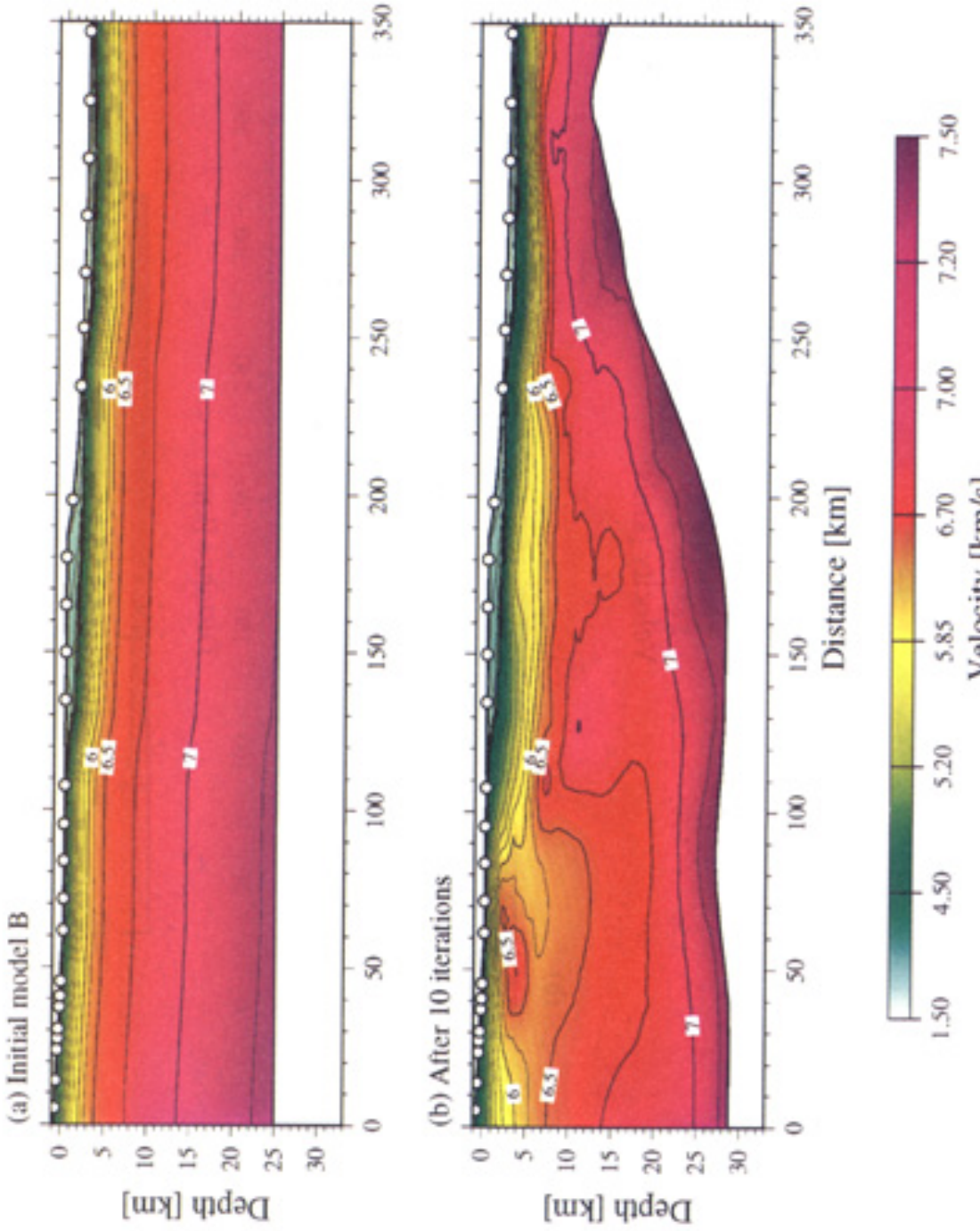

Plate 2. Result of tomographic inversion with a different starting model. (a) Initial model constructed by hanging the 1-D average crustal velocity profile of the model shown in Plate 1a beneath the basement. Initial Moho is flat at a depth of 25 km. (b) After 10 iterations RMS travel time misfit was reduced to 78 ms with χ^2 of 1.01.

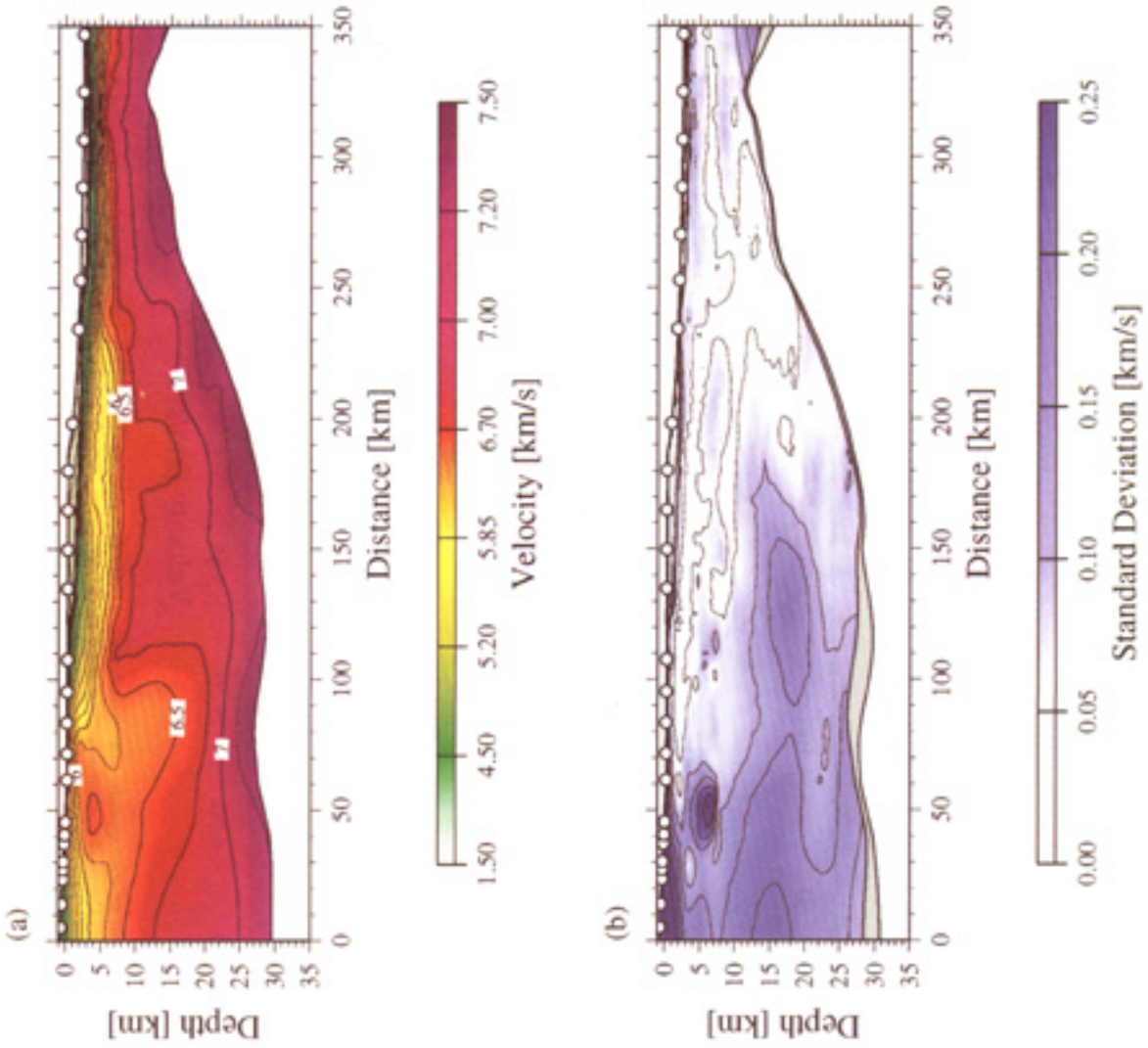

Plate 3. (a) Final velocity model derived by averaging all Monte Carlo ensembles. (b) Corresponding standard deviation for velocity and depth nodes. Contours are drawn at 0.05 km/s interval.

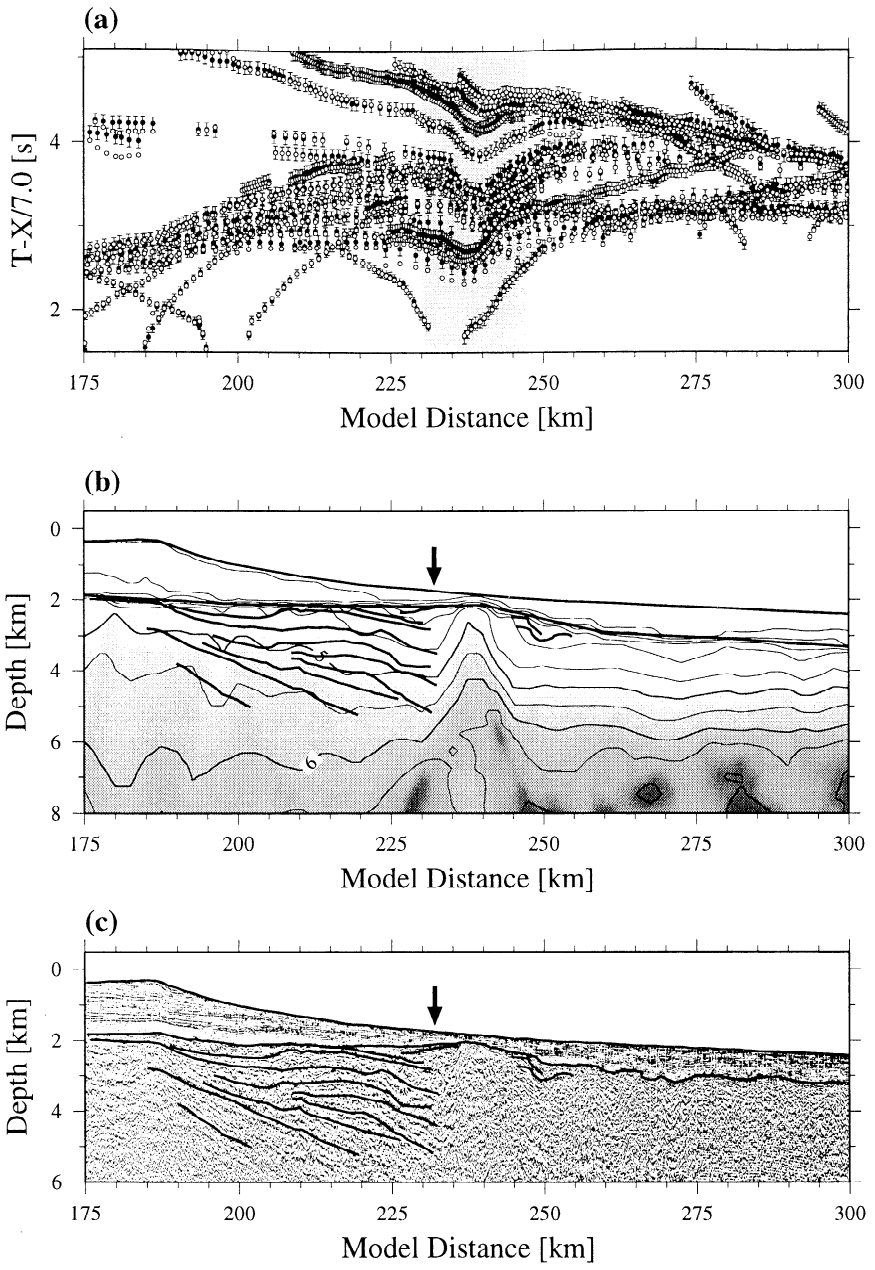

Figure 12. Short-wavelength features derived by inverting with shorter correlation lengths. (a) Observed travel times (solid circle with error bar) plotted with predicted travel times (open circle) based on the high-resolution model shown in Figure 12b. Better fits are obtained for bumps in travel times around km 230-245. (c) Depth-migrated section of seismic reflection data overlaid with line drawing. The seaward end of the wedge of seaward dipping reflectors (shown by arrows in Figures 12b and 12c) correlates well with the high-velocity anomaly.

Our refraction and reflection tomographic method has several distinct advantages over existing codes, in that it (1) incorporates reflection tomography; (2) is able to quantify the velocity-depth ambiguity associated with reflection travel times; (3) allows explicit error analysis in velocity and reflector depth using a broad model space (Plate 3); (4) allows rays to be traced to all observations regardless of model complexity; and (5) is not limited to an a coarse model parameterization, which can result in an unrealistic estimate of model uncertainty. Our approach thus incorporates elements that have previously not been combined in any single existing method [e.g., *Zelt and Smith*, 1992; *Van Avendonk et al.*, 1998; *Zhang et al.*, 1998] and produces an efficient, stable result with quantifiable error bounds.

Although tomographic methods have been mainly used to resolve small-scale velocity structures, we should also use them to construct large-scale crustal velocity models. It is important to use a tomographic method with a robust uncertainty analysis, such as the Monte Carlo method used in this study, especially when the geological interpretation of a velocity model critically depends on the absolute values of estimated parameters. Without knowing their realistic uncertainties, it would be difficult to judge the fidelity of such an interpretation.

5.3. Interpretation of Long-Wavelength Velocity Structure

Our interpretation of the continent-ocean transition zone is shown in Figure 13a. The stretched continental crust extends over

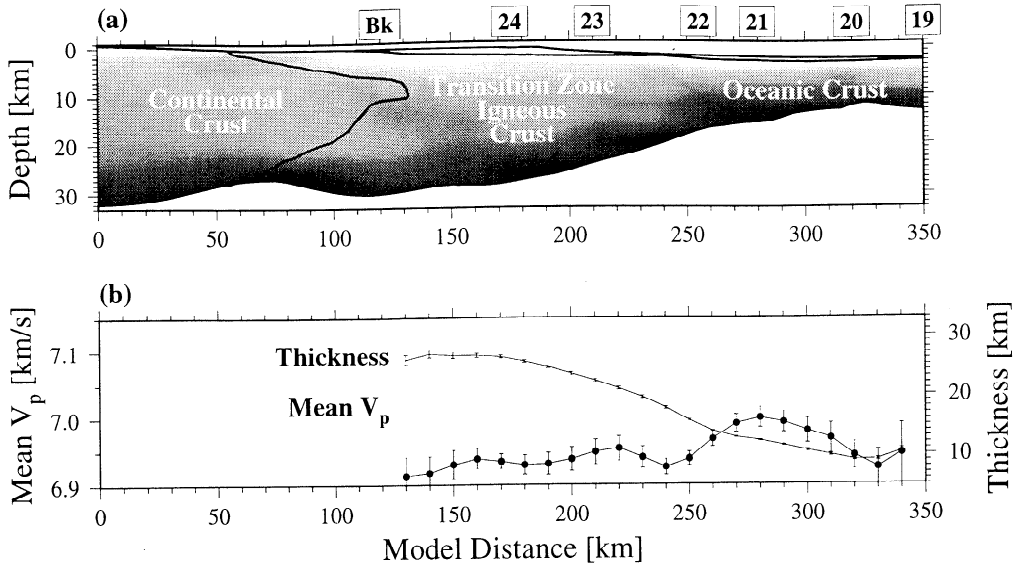

Figure 13. (a) Geological interpretation of the long-wavelength velocity model of Plate 3a. Solid line denotes the seaward extent of the stretched continental crust. Magnetic anomalies chron 19 to 24 identified on other southern transects are projected on this transect to provide age control. Bk denotes the breakup point interpreted by Holbrook et al. (submitted manuscript, 2000). (b) Mean velocity and thickness of the igneous crustal part calculated at 10-km interval with 20-km-wide averaging window, using the 100 Monte Carlo ensembles.

50 km below the extrusive layer, showing a similar geometry to other transects across the North Atlantic continental margins [*White et al.*, 1987; *Barton and White*, 1997a; Holbrook et al., submitted manuscript, 2000]. Given the smoothed nature of the tomographic image, the actual continent-ocean boundary could be sharper, as observed for the U.S. Atlantic margin [*Holbrook et al.*, 1994a, 1994b; *Lizarralde and Holbrook*, 1997], but we use the diffuse boundary shown in Figure 13a to obtain a conservative estimate of the volume of igneous products. As did Holbrook et al. (submitted manuscript, 2000), we calculate the thickness and the mean velocity of the igneous crust as a function of the model distance (Figure 13b). Velocities and depths within a horizontal window of 20 km were averaged at each model distance, and we repeated this averaging procedure with the 100 Monte Carlo ensembles to estimate uncertainty.

Using these velocities and crustal thicknesses, we can place a first-order constraint on the style of mantle melting during continental breakup. Following the procedure described by Holbrook et al. (submitted manuscript, 2000), a predicted relationship between the mean crustal velocity and crustal thickness with the corresponding mantle potential temperatures is plotted for a passive upwelling case and three active upwelling cases, with active upwelling ratio of 2, 4, and 8 (Figure 14). The active upwelling ratio is defined as the mantle upwelling rate

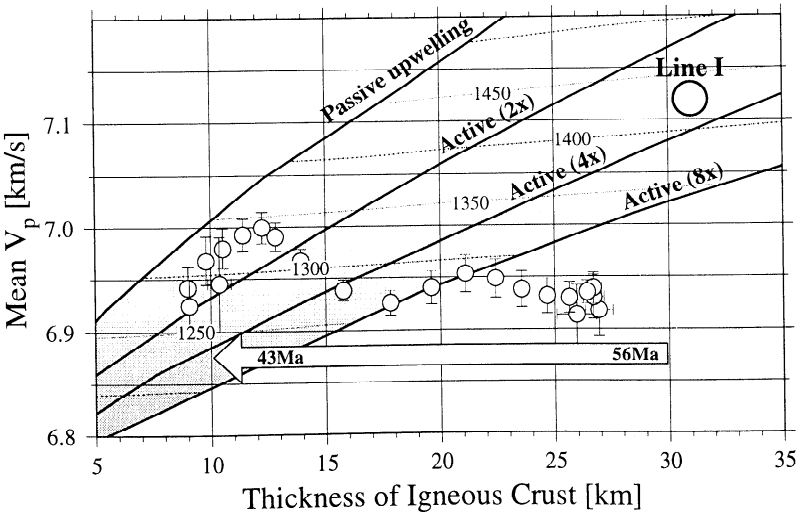

Figure 14. Mean velocity of the igneous crust plotted as a function of corresponding thickness (open circles with error bars). The large open circle indicates the range of the velocity-thickness data (which are nearly constant) for transect 1. Also shown are the predicted velocity-thickness curves based on the mantle melting model for passive and three active upwelling cases. The contours of corresponding mantle potential temperature are drawn at 50°C interval.

normalized by the surface divergence half rate. One prominent feature of the observed mean velocity is that it is confined in a narrow range from 6.92 to 7.00 km/s, regardless of the corresponding crustal thickness (Figure 14). This translates into a relatively constant mantle potential temperature (1270-1340°C), with a drastic temporal variation in the active upwelling ratio from ~8 during the initial phase of breakup to ~1 (passive) after ~43 Ma. Interestingly, this is the same range of upwelling ratios obtained by *Kelemen and Holbrook* [1995] for the U.S. East Coast. In contrast, the velocity-thickness data from transect 1 suggest active upwelling of high-temperature (1400-1450°C) mantle throughout the opening of the North Atlantic (Figure 14). The uncertainty in average velocity based on the Monte Carlo method is sufficiently small to clearly define this marked velocity contrast between the two adjacent transects. Though the transect 1 data may be consistent with its coincidence with the presumed hotspot track, it is puzzling, from a viewpoint of a mantle plume hypothesis, that the more vigorous active upwelling of a cooler mantle during the initial rifting period is inferred for a location only 250 km from the presumed center of the hotspot track. The influence of the Iceland plume during the breakup of Greenland and Europe therefore may have been spatially restricted, and some contribution from nonplume components, such as in the convection models proposed by *Mutter et al.* [1988] and *Boutilier and Keen* [1999], may be required to account for the inferred complexity in the thermal and dynamic state of the mantle during the continental breakup.

6. Summary

Using the multichannel and wide-angle seismic data obtained in the 1996 SIGMA experiment across the southeast Greenland margin, we were able to resolve crustal structure along the 350-km-long transect, including nearly undeformed continental crust, thick igneous crust at the continent-ocean transition zone, and moderately thick oceanic crust near the seaward end. The depth-migrated MCS section clearly images the basement topography and the shallow crustal reflectivity, including seaward dipping reflectors. We developed a new tomographic method to invert wide-angle refraction and reflection travel time data for the long-wavelength structure along the entire transect. Strong lateral heterogeneity both in velocity and reflector depth is recovered, and the Monte Carlo uncertainty analysis shows that the most of the model parameters are well constrained, with 0.05-0.10 km/s error for velocity nodes and 0.25-1.5 km error for depth nodes. Negligible trade-off between velocity and depth is also demonstrated.

The lateral variation in the mean velocity and thickness of the igneous crust is interpreted as a temporal variation in the composition and the volume of mantle melt produced during the opening of the North Atlantic. On the basis of a simple mantle melting model incorporating the effect of active upwelling, the inferred melt composition and volume seem to require a gradual transition from vigorous active upwelling during the initial stage of opening (56-50 Ma) to passive upwelling after 43 Ma, with moderately high potential temperatures of 1270-1340°C. This result makes a sharp contrast to the almost unvarying active upwelling of high-temperature mantle inferred for transect 1, which is on the presumed Iceland hotspot track located ~250 km north of transect 2. This contrast may suggest a limited influence of the Iceland plume on the rifting magmatism and a considerable nonplume component in the mantle.

Acknowledgments. We gratefully acknowledge the captain and crew of the R/V *Maurice Ewing* for their cooperation. We thank Rob Handy, Jim Doran, and Dave DuBois for WHOI OBH data acquisition, Bob Busby for USGS OBS data acquisition, Paul Henkart for onboard MCS data processing, and Stefan Bernstein for on-land field work. Dan Lizarralde, Harm Van Avendonk, Rafi Katzman, and Tom Jordan were always helpful for constructive discussion. We also thank Colin Zelt and two anonymous reviewers for a number of helpful comments and suggestions. This work was supported by NSF grant OCE-9416631.

References

Aki, K., and P.G. Richards, *Quantitative Seismology*, W. H. Freeman, New York, 1980.

Barton, A.J., and R.S. White, Crustal structure of Edoras Bank continental margin and mantle thermal anomalies beneath the North Atlantic, *J. Geophys. Res.*, *102*, 3109-3129, 1997a.

Barton, A.J., and R.S. White, Volcanism on the Rockall continental margin, *J. Geol. Soc. London*, *154*, 531-536, 1997b.

Bickel, S.H., Velocity-depth ambiguity of reflection traveltimes, *Geophysics*, *55*, 266-276, 1990.

Bishop, T.N., K.P. Bube, R.T. Cutler, R.T. Langan, P.L. Love, J.R. Resnick, R.T. Shuey, D.A. Spindler, and H.W. Wyld, Tomographic determination of velocity and depth in laterally varying media, *Geophysics*, *50*, 903-923, 1985.

Boutilier, R.R., and C.E. Keen, Small-scale convection and divergent plate boundaries, *J. Geophys. Res.*, *104*, 7389-7403, 1999.

Brandsdóttir, B., W. Menke, P. Einarsson, R.S. White, and R.K. Staples, Færoe-Iceland Ridge Experiment, 2, Crustal structure of the Krafla central volcano, *J. Geophys. Res.*, *102*, 7867-7886, 1997.

Bube, K.P., R.T. Langan, and J.R. Resnick, Theoretical and numerical issues in the determination of reflector depths in seismic reflection tomography, *J. Geophys. Res.*, *100*, 12,449-12,458, 1995.

Christensen, N.I., and W.D. Mooney, Seismic velocity structure and composition of the continental crust: A global view, *J. Geophys. Res.*, *100*, 9761-9788, 1995.

Coffin, M.F., and O. Eldholm, Large igneous provinces: Crustal structure, dimensions, and external consequences, *Rev. Geophys.*, *32*, 1-36, 1994.

Deal, M.M., and G. Nolet, Nullspace shuttles, *Geophys. J. Int.*, *124*, 372-380, 1996.

Dijkstra, E.W., A note on two problems in connection with graphs, *Numer. Math.*, *1*, 269-271, 1959.

Eldholm, O., J. Thiede, and E. Taylor, The Norwegian continental margin: Tectonics, volcanic and paleoenvironmental framework, *Proc. Ocean Drill. Program Sci. Results*, *104*, 5-26, 1989.

Fischer, R., and J.M. Lees, Shortest path ray tracing with sparse graphs, *Geophysics*, *58*, 987-996, 1993.

Gallo, G., and S. Pallottino, Shortest path methods: A unifying approach, *Math. Program. Study*, *26*, 38-64, 1986.

Hestenes, M.R., Pseudoinverses and conjugate gradients, *Commun. ACM*, *18*, 40-43, 1975.

Hill, R.I., I.H. Campbell, G.F. Davies, and R.W. Griffiths, Mantle plumes and continental tectonics, *Science*, *256*, 186-193, 1992.

Hinz, K., A hypothesis on terrestrial catastrophes wedges of very thick oceanward dipping layers beneath passive continental margins, *Geol. Jahrb., Reihe E*, *22*, 3-28, 1981.

Holbrook, W.S., and P.B. Kelemen, Large igneous province on the US Atlantic margin and implications for magmatism during continental breakup, *Nature*, *364*, 433-436, 1993.

Holbrook, W.S., G.M. Purdy, R.E. Sheridan, L. Glover III, M. Talwani, J. Ewing, and D. Hutchinson, Seismic structure of the U.S. Mid-Atlantic continental margin, *J. Geophys. Res.*, *99*, 17,871-17,891, 1994a.

Holbrook, W.S., E.C. Reiter, G.M. Purdy, D. Sawyer, P.L. Stoffa, J.A. Austin, Jr., J. Oh, and J. Makris, Deep structure of the U.S. Atlantic continental margin, offshore South Carolina, from coincident ocean bottom and multichannel seismic data, *J. Geophys. Res.*, *99*, 9155-9178, 1994b.

Kelemen, P.B., and W.S. Holbrook, Origin of thick, high-velocity igneous crust along the U.S. East Coast Margin, *J. Geophys. Res.*, *100*, 10,077-10,094, 1995.

Kinzler, R.J., and T.L. Grove, Primary magmas of mid-ocean ridge basalts, 2, Applications, *J. Geophys. Res.*, *97*, 6907-6926, 1992.

Korenaga, J., Magmatism and dynamics of continental breakup in the presence of a mantle plume, Ph.D. thesis, MIT/WHOI Joint Program, Cambridge, Mass., 2000.

Langmuir, C.H., E.M. Klein, and T. Plank, Petrological systematics of mid-ocean ridge basalts: Constraints on melt generation beneath ocean ridges, in *Mantle Flow and Melt Generation at Mid-Ocean Ridges, Goephys. Monogr. Ser.*, vol. 71, edited by J. Phipps Morgan, D.K. Blackman, and J.M. Sinton, pp. 183-280, AGU, Washington, D. C., 1992.

Larsen, H.C., and R.A. Duncan, Introduction: Leg 163 background and objectives, *Proc. Ocean Drill. Program Initial Rep.*, *163*, 5-13, 1996.

Larsen, H.C., and S. Jakobsdóttir, Distribution, crustal properties and significance of seawards-dipping sub-basement reflectors off E Greenland, in *Early Tertiary Volcanism and the Opening of the NE Atlantic*, edited by A.C. Morton, and L.M. Parson, *Geol. Soc. Spec. Publ.*, *39*, 95-114, 1988.

Larsen, H.C., A.D. Saunders, P.D. Clift, and the Shipboard Scientific Party, *Proceedings of the Drilling Program Initial Report*, vol. 152, Ocean Drill. Program, College Station, Tex., 1994.

Lizarralde, D., and W.S. Holbrook, U.S. Mid-Atlantic margin structure and early thermal evolution, *J. Geophys. Res.*, *102*, 22,855-22,875, 1997.

Matarese, J.R., Nonlinear traveltime tomography, Ph.D. thesis, Mass. Inst. of Technol., Cambridge, 1993.

McKenzie, D., and M.J. Bickle, The volume and composition of melt generated by extension of the lithosphere, *J. Petrol.*, *29*, 625-679, 1988.

Moser, T.J., Shortest path calculation of seismic rays, *Geophysics*, *56*, 59-67, 1991.

Moser, T.J., G. Nolet, and R. Snieder, Ray bending revisited, *Bull. Seismol. Soc. Am.*, *82*, 259-288, 1992.

Mutter, J.C., and C.M. Zehnder, Deep crustal structure and magmatic processes: The inception of seafloor spreading in the Norwegian-Greenland Sea, in *Early Tertiary Volcanism and the Opening of the NE Atlantic*, edited by A.C. Morton, and L.M. Parson, *Geol. Soc. Spec. Publ.*, *39*, 35-48, 1988.

Mutter, J.C., M. Talwani, and P.L. Stoffa, Origin of seaward-dipping reflectors in oceanic crust off the Norwegian margin by "subaerial seafloor spreading," *Geology*, *10*, 353-357, 1982.

Mutter, J.C., W.R. Buck, and C.M. Zehnder, Convective partial melting, 1, A model for the formation of thick basaltic sequences during the initiation of spreading, *J. Geophys. Res.*, *93*, 1031-1048, 1988.

Nakamura, Y., P.L. Donoho, P.H. Roper, and P.M. McPherson, Large-offset seismic surveying using ocean-bottom seismograms and air guns: Instrumentation and field technique, *Geophysics*, *52*, 1601-1611, 1987.

Nakanishi, I., and K. Yamaguchi, A numerical experiment on nonlinear image reconstruction from first-arrival times for two-dimensional island arc structure, *J. Phys. Earth*, *34*, 195-201, 1986.

Paige, C.C., and M.A. Saunders, LSQR: An algorithm for sparse linear equations and sparse least squares, *Trans. Math. Software*, *8*, 43-71, 1982.

Papazachos, C., and G. Nolet, *P* and *S* deep velocity structure of the Hellenic area obtained by robust nonlinear inversion of travel times, *J. Geophys. Res.*, *102*, 8349-8367, 1997.

Prothero, W.A., W.J. Taylor, and J.A. Eickemeyer, A fast, two-point, three-dimensional raytracing algorithm using a simple step search method, *Bull. Seismol. Soc. Am.*, *78*, 1190-1198, 1988.

Richards, M.A., R.A. Duncan, and V.E. Courtillot, Flood basalts and hot-spot tracks: Plume heads and tails, *Science*, *246*, 103-107, 1989.

Roberts, D.G., J. Backman, A.C. Morton, J.W. Murray, and J.B. Keene, Evolution of volcanic rifted margins: Synthesis of Leg 81 results on the west margin of Rockall Plateau, *Initial Rep. Deep Sea Drill. Proj.*, *81*, 883-911, 1984.

Ross, W.S., The velocity-depth ambiguity in seismic traveltime data, *Geophysics*, *59*, 830-843, 1994.

Scales, J.A., and R. Snieder, To Bayes or not to Bayes?, *Geophysics*, *62*, 1045-1046, 1997.

Shaw, P.R., and J.A. Orcutt, Waveform inversion of seismic refraction data and applications to young Pacific crust, *Geophys. J. R. Astron. Soc.*, *82*, 375-414, 1985.

Srivastava, S.P., and C.R. Tapscott, Plate kinematics of the North Atlantic, in *The Geology of North America*, vol. M, *The Western North Atlantic Region*, edited by P.R. Vogt and B.E. Tucholke, pp. 379-404, Geol. Soc. of Am., Boulder, Colo., 1986.

Staples, R.K., R.S. White, B. Brandsdóttir, W. Menke, P.K.H. Maguire, and J.H. McBride, Färoe-Iceland Ridge Experiment, 1, Crustal structure of northeastern Iceland, *J. Geophys. Res.*, *102*, 7849-7866, 1997.

Stoffa, P.L., J.T. Fokkema, R.M. de Luna Freire, and W.P. Kessinger, Split-step Fourier migration, *Geophysics*, *55*, 410-421, 1990.

Stork, C., Singular value decomposition of the velocity-reflector depth tradeoff, part 1, Introduction using a two-parameter model, *Geophysics*, *57*, 927-932, 1992a.

Stork, C., Singular value decomposition of the velocity-reflector depth tradeoff, part 2, High-resolution analysis of a generic model, *Geophysics*, *57*, 933-943, 1992b.

Stork, C., and R.W. Clayton, Linear aspects of tomographic velocity analysis, *Geophysics*, *56*, 483-495, 1991.

Tarantola, A., *Inverse Problem Theory: Methods for Data Fitting and Model Parameter Estimation*, 613 pp., Elsevier Sci., New York, 1987.

Tarantola, A., and B. Valette, Inverse problems = quest for information, *J. Geophys.*, *50*, 159-170, 1982.

Toomey, D.R., and G.R. Foulger, Tomographic inversion of local earthquake data from the Hengill-Grensdalur central volcano complex, Iceland, *J. Geophys. Res.*, *94*, 17,497-17,510, 1989.

Toomey, D.R., S.C. Solomon, and G.M. Purdy, Tomographic imaging of the shallow crustal structure of the East Pacific Rise at 9°30'N, *J. Geophys. Res.*, *99*, 24,135-24,157, 1994.

Um, J., and C. Thurber, A fast algorithm for two-point seismic ray tracing, *Bull. Seismol. Soc. Am.*, *77*, 972-986, 1987.

Van Avendonk, H.J.A., An investigation of the crustal structure of the Clipperton transform fault area using 3D seismic tomography, Ph.D. thesis, Univ. of Calif., San Diego, 1998.

Van Avendonk, H.J.A., A.J. Harding, and J.A. Orcutt, A two-dimensional tomographic study of the Clipperton transform fault, *J. Geophys. Res.*, *103*, 17,885-17,899, 1998.

Vidale, J., Finite-difference calculation of travel times, *Bull. Seismol. Soc. Am.*, *78*, 2062-2076, 1988.

White, D.J., and R.M. Clowes, Shallow crustal structure beneath the Juan de Fuca Ridge from 2-D seismic refraction tomography, *Geophys. J. Int.*, *100*, 349-367, 1990.

White, R., and D. McKenzie, Magmatism at rift zones: The generation of volcanic continental margins and flood basalts, *J. Geophys. Res.*, *94*, 7685-7729, 1989.

White, R.S., G.D. Spence, S.R. Fowler, D.P. McKenzie, G.K. Westbrook, and A.N. Bowen, Magmatism at rifted continental margins, *Nature*, *330*, 439-444, 1987.

White, R.S., D. McKenzie, and R.K. O'Nions, Oceanic crustal thickness from seismic measurements and rare earth element inversions, *J. Geophys. Res.*, *97*, 19,683-19,715, 1992.

Yilmaz, Ö., *Seismic Data Processing*, 526 pp., Soc. of Exp. Geophys., Tulsa, Okla., 1987.

Zelt, C.A., and R.B. Smith, Seismic traveltime inversion for 2-D crustal velocity structure, *Geophys. J. Int.*, *108*, 16-34, 1992.

Zhang, J., Nonlinear refraction and reflection traveltime tomography, Ph.D. thesis, Mass. Inst. of Technol., Cambridge, 1997.

Zhang, J., and M.N. Toksöz, Nonlinear refraction traveltime tomography, *Geophysics*, *63*, 1726-1737, 1998.

Zhang, J., U.S. ten Brink, and M.N. Toksöz, Nonlinear refraction and reflection travel time tomography, *J. Geophys. Res.*, *103*, 29,743-29,757, 1998.

R. S. Detrick and P. B. Kelemen, Department of Geology and Geophysics, Woods Hole Oceanographic Institution, Woods Hole, MA 02543. (rdetrick@whoi.edu; pkelemen@whoi.edu)

W. S. Holbrook, Department of Geology and Geophysics, University of Wyoming, Laramie, WY 82071-3006. (steveh@uwyo.edu)

J. R. Hopper, T. Dahl-Jensen, and H. C. Larsen, Danish Lithosphere Centre, DK-1350 Copenhagen, Denmark. (jrh@dlc.ku.dk; tdj@dlc.ggu.min.dk; larsenhc@dlc.ggu.min.dk)

G. M. Kent, IGPP – 0225, Scripps Institution of Oceanography, University of California, 9500 Gilman Drive, San Diego, CA 92093. (gkent@eos.ucsd.edu)

J. Korenaga, Department of Earth, Atmospheric, and Planetary Sciences, Massachusetts Institute of Technology, Room 54-522, Cambridge, MA 02139. (korenaga@mit.edu)

(Received September 2, 1999; revised May 24, 2000;
accepted May 30, 2000.)